Published in final edited form as:
Nat Struct Mol Biol. 2019 December 01; 26(12): 1141–1150. doi:10.1038/s41594-019-0332-9.

The structure and oxidation of the eye lens chaperone αA-crystallin

Christoph J. O. Kaiser[#1], **Carsten Peters**[#1], **Philipp W. N. Schmid**[1], **Maria Stavropoulou**[1,2], **Juan Zou**[3], **Vinay Dahiya**[1], **Evgeny V. Mymrikov**[1,6], **Beate Rockel**[1], **Sam Asami**[1,2], **Martin Haslbeck**[1], **Juri Rappsilber**[3,4], **Bernd Reif**[1,2], **Martin Zacharias**[5], **Johannes Buchner**[1,*], **Sevil Weinkauf**[1,*]

[1]Center for Integrated Protein Science Munich at the Department Chemie, Technische Universität München, Garching, Germany

[2]Institute of Structural Biology, Helmholtz Zentrum München, Neuherberg, Germany

[3]Wellcome Centre for Cell Biology, University of Edinburgh, Edinburgh, United Kingdom

[4]Bioanalytics, Institute of Biotechnology, Technische Universität Berlin, Berlin, Germany

[5]Center for Integrated Protein Science Munich at the Physics Department, Technische Universität München, Garching, Germany

[#] These authors contributed equally to this work.

Abstract

The small heat shock protein (sHsp) αA-crystallin is a molecular chaperone important for the optical properties of the vertebrate eye lens. It forms heterogeneous oligomeric ensembles. We determined the structures of human αA-crystallin oligomers combining cryo-electron microscopy, cross-linking/mass spectrometry, nuclear magnetic resonance spectroscopy and molecular modeling. The different oligomers can be interconverted by the addition or subtraction of tetramers, leading to mainly 12-, 16- and 20-meric assemblies in which interactions between N-terminal regions are important. Cross-dimer domain-swapping of the C-terminal region is a determinant of αA-crystallin heterogeneity. Human αA-crystallin contains two cysteines, which can form an intramolecular disulfide *in vivo*. Oxidation *in vitro* requires conformational changes and oligomer dissociation. The oxidized oligomers, which are larger than reduced αA-crystallin

[*]**Correspondence to:** sevil.weinkauf@tum.de; johannes.buchner@tum.de.
[6] **Present address:** Institute for Biochemistry and Molecular Biology, Albert-Ludwigs-Universität Freiburg, Stefan-Meier-Straße 17, 79104 Freiburg, Germany

Author Contributions

C.J.O.K., J.B. and S.W. designed and conceived the research plan. C.P., B. Rockel. and C.J.O.K. performed electron microscopy experiments and processed the data. C.J.O.K. carried out, with contributions from P.W.N.S., E.V.M. and M.H., the experiments for the biochemical and biophysical characterization. V.D. provided full-length human recombinant p53. M.S. and S.A. performed NMR experiments. M.S. and B. Reif analyzed the NMR data. J.Z. conducted cross-linking/mass spectrometry experiments. J.Z. and J.R. analyzed the cross-linking data. M.Z. performed molecular dynamics simulations and model building. C.J.O.K., J.B. and S.W. wrote the manuscript with input from all authors.

Competing Interests

The authors declare no competing interests.

Europe PMC Funders Author Manuscripts

and destabilized against unfolding, are active chaperones and can transfer the disulfide to destabilized substrate proteins. This insight into the structure and function of αA-crystallin provides a basis for understanding its role in the eye lens.

Introduction

The small heat shock proteins (sHsps) αA- and αB-crystallin are major constituents of the vertebrate eye lens[1]. They ensure lens transparency[1,2] and prevent lens proteins from aggregation[3,4]. Mutations in both α-crystallins result in cataracts and in a variety of eye disorders, emphasizing their importance for the lens[2,5]. Besides the commonality of the processes in which αA- and αB-crystallin are involved, differences in their distribution in the lens and expression patterns exist[6–9]. Specifically, αA-crystallin is predominantly expressed in the eye lens. *In vitro* studies point towards mechanistic differences between αA- and αB-crystallin in suppressing the aggregation of model substrates[10,11], and mutations of conserved residues have different impact on the two crystallins[12].

Human αA-crystallin, a 19.9 kDa protein with 173 residues, consists of three structurally distinct regions: the conserved α-crystallin domain (ACD, residues 61-145) flanked by the N-terminal region (NTR, residues 1-60) and the short, flexible C-terminal region (CTR, residues 146-173)[13,14]. The ACD adopts a β-sandwich fold composed of two anti-parallel sheets of three and four β-strands, respectively. It dimerizes through the interaction of the β6+7-strands of two adjacent protomers ('β7-interface dimer')[15,16]. αA-crystallin assembles into polydisperse oligomers with extensive size heterogeneity and a constant exchange of subunits between oligomers[17–19]. There is, as yet, no structural information available either for full-length αA-crystallin or for αA-crystallin in any oligomeric form. Consequently, the structural elements critical for assembly and those conferring plasticity to the oligomeric assembly are poorly understood. The involvement of the NTR in oligomer formation is indicated by the shift of the average oligomer ensemble to smaller species, dimers and/or tetramers, upon its truncation[20–23]. Studies on C-terminal truncation mutants of αA-crystallin from different organisms display significant disparities, leaving the role of the CTR in oligomer formation still ill defined[18,21,24–27]. The CTR of αA-crystallin exhibits greater overall flexibility than that of αB-crystallin[28], including the segment containing the conserved IXI motif, which promotes oligomer formation by binding into the β4/β8 groove within the ACD of a neighboring protomer[29,30].

A characteristic of human αA-crystallin is the presence of two cysteines in its ACD, the invariant C131 (found in most species) and an additional cysteine at position 142 also found in αA-crystallin from primates and zebrafish (*Danio rerio*)[31]. C131 was predicted to be buried, whereas C142 was suggested to be fully solvent-exposed[32,33]. In the crystal structure of the zebrafish αA-crystallin ACD, the CTR covers C132 while leaving C143 accessible[16]. Notably, already in young human lenses and during the first ~30 years of life, ~45% of αA-crystallin has an intramolecular disulfide bond (henceforth denoted as oxidized αA-crystallin, αA_{ox}), while in the remaining fraction the cysteines are in the free sulfhydryl form (reduced αA-crystallin, αA_{red})[34–37]. In young lenses, a subpopulation might form intermolecular disulfides as well[38]. With ageing, the amount of αA_{ox} increases up to 90%[36]

Europe PMC Funders Author Manuscripts

and it becomes a major constituent of high molecular weight aggregates[39–41], concomitant with an age-dependent loss of the chaperone activity of α-crystallin[42]. αA_{red} is undetectable in cataractous lenses[35]. Despite their importance, the structural and functional consequences of αA-crystallin oxidation are as yet unknown.

Here we present the architecture and plasticity of human αA-crystallin oligomers as well as the structural and functional consequences of its oxidation. The structures of human αA-crystallin assemblies and pseudoatomic models of a 16-meric assembly reveal the domain-swapping of the CTR to be a key determinant of αA-crystallin heterogeneity. Formation of the intramolecular disulfide bond leads to distinct oligomers that are chaperone active and can transfer their intramolecular disulfides to destabilized substrate proteins.

Results

Oligomer architecture and conformational heterogeneity of reduced αA-crystallin

To determine the oligomer architecture of reduced human αA-crystallin, we employed single-particle cryo-EM (Extended Data Fig. 1). The initial analysis of ~74,000 projection images revealed two distinct populations, one containing round particles with 3-, 4- and 5-fold symmetries and diameters varying between 6 and 16 nm (Extended Data Fig. 1b), the other comprising elongated structures with 2-fold symmetry and a nearly uniform long axis of 13-14 nm (Extended Data Fig. 1c). The two populations seemed to represent end- and side-on projections of a barrel-like architecture with varying subunit stoichiometries. On this basis, we established a three-dimensional (3D) reconstruction procedure that allowed us to assign ~80% of the particles to 12-, 16- and 20-meric assemblies with abundances of approximately 36%, 27% and 19% and calculate the corresponding 3D models (Fig. 1) at resolutions of 9.2 Å, 9.8 Å and 9.0 Å, respectively (Extended Data Fig. 1h, Table 1).

According to the reconstructed EM volumes (Fig. 1), all three assemblies form hollow, barrel-like structures with a recurring unit resembling a tilted ‘Z’ comprising two substructures that are connected in the mid-plane of the barrel. Each of these substructures is large enough to accommodate an αA-crystallin dimer, implying that the Z-shaped structures represent tetramers (dimers of dimers), which serve as the building blocks of the oligomers. Notably, in the average structures of the 12- and 16-mers, adjacent tetramers are not connected in the equatorial plane of the barrel (Fig. 1a,b) whereas there is a well-resolved density bridging neighboring tetramers in the 20-mer (Fig. 1c).

To elucidate the structural variability of αA_{red} oligomers, each oligomer population was subjected to 3D sampling and classification, which revealed that the density corresponding to an αA-crystallin dimer remains almost invariant within all three populations (Extended Data Fig. 2). In contrast, significant heterogeneity exists in areas where adjacent tetramers come together in apical and equatorial regions which most likely harbor the N- and/or C-termini. The oligomers differ in the density connecting the tetramers in the equatorial plane: this density is lacking in all sub-ensembles of the 12-mer population, while it is present in approximately 30% of the 16-mer population and in all sub-ensembles of the 20-mer population (Extended Data Fig. 2 and Supplementary Table 1). The observed heterogeneity is suggestive of dynamic inter-subunit interactions involving N- and/or C-terminal regions.

This conformational heterogeneity, together with very similar projection views of different oligomers, presumably limits the resolution of the reconstructions.

Pseudoatomic model of the αA-crystallin 16-mer

To obtain pseudoatomic models of the αA_{red} 16-mer, we subjected full-length protein to cross-linking and mass spectrometry. Using the cross-linker bis(sulfosuccinimidyl)suberate (BS3), we identified numerous intra- and intermolecular cross-links (Extended Data Figs. 3,4 and Supplementary Table 2). The data demonstrated the structural similarity of human αA-crystallin in its ACD and CTR to zebrafish and bovine αA-crystallin, as all distances between corresponding residue pairs resolved in the respective crystal structures were below 30 Å - approximately the upper distance limit dictated by the utilized cross-linker[43] (Extended Data Fig. 4f).

The volume of the equatorial inter-tetramer density present in some 16-mer subpopulations is just large enough to accommodate the CTR (Extended Data Fig. 2). Together with its positioning, we concluded that the variability within this area stems from 3D domain-swapping of the CTR: in structural classes containing the equatorial inter-tetramer density, the IPV (the sequence of the IXI motif in αA-crystallin) motif binds intermolecularly into the β4/β8 pocket of an adjacent protomer (3D domain-swapped configuration), while in classes lacking the density, it binds intramolecularly into the β4/β8 pocket of the same polypeptide chain (non-3D domain-swapped configuration). This view is supported by the occurrence of the CTRs in swapped and non-swapped configurations in bovine and zebrafish αA-crystallin ACD crystal structures, respectively[15,16]. Thus, we generated pseudoatomic models of the αA_{red} 16-mer with the CTRs in both configurations using (I) shape and symmetry constraints from the cryo-EM envelopes differing in the equatorial inter-tetramer density, (II) the crystal structures of truncated versions of bovine and zebrafish αA-crystallins as templates, and (III) intra- and intermolecular distance restraints from cross-linking. During modeling using molecular dynamics flexible fitting, a homology-modeled structure for the NTR (residues 1-60) was used that contained three short helices connected by flexible loops (Extended Data Fig. 5a,b). The structures of the central ACD (residues 61-145) and part of the CTR (residues 146-166) were derived from homology modeling based on the above-mentioned crystal structures. The residues 167-173 were not included in the model due to their flexibility[28]. The fitting procedure resulted in an ensemble of solutions with the NTRs of both apical (M_{ap}) and equatorial (M_{eq}) protomers adopting a variety of possible conformations (Extended Data Fig. 5c,d), consistent with their flexibility. Although no consensus structure could be derived for the NTR, its integration during the fitting process was crucial because it restricted the positioning of the central ACD and CTR. The best structures were selected based on RMSD, stereochemistry and cross-correlation with respect to the cryo-EM density and further energy minimized.

In the final pseudoatomic models of the αA_{red} 16-mer (Fig. 2) that fit best into the EM-map from all possible models and fulfill cross-linking restraints, all parts of the polypeptide chain are accommodated within the electron density. The models reveal that two protomers form a β7-interface dimer. Interactions between N-termini mediate the association of two dimers across the equator to form a tetramer (equatorial N-terminal interface, eq-NI, Fig. 2a,d),

which is the recurring unit of the oligomer. Further N-terminal interactions between apical protomers of the tetramers (apical N-terminal interface, ap-NI) serve to form the 16-mer (Fig. 2a). The close proximity of the N-terminal segments is corroborated by intermolecular cross-links involving residues M1, K11 and T13 (Supplementary Table 2), which are all satisfied in our models. In contrast to the prevailing contribution of the NTR to oligomer formation, the CTR is barely involved in inter-subunit interactions. In both 16-mer models (Fig. 2a,b), the CTRs of M_{ap} are in a non-3D domain-swapped configuration as the distance between apical protomers is too large compared to the length of the CTR to permit an intermolecular IXI-β4/β8 interaction. On the other hand, although the distance between M_{eq} of neighboring tetramers supports this interaction in both potential directionalities of the IPV sequence, the CTR contributes to the assembly by 3D domain-swapping in only ~30% of the 16-mer population (Fig. 2b,f). 3D domain-swapping creates an interface (equatorial C-terminal interface, eq-CI) in which the CTRs of M_{eq} from neighboring tetrameric units are in close proximity, consistent with the observed intermolecular cross-link K166-K166 (not used as a modeling constraint), and interact through electrostatic interactions involving residues downstream of the IXI motif (Fig. 2b,f).

3D domain-swapping of the C-terminal region in the αA-crystallin ensemble

The 12- and 20-meric αA_{red} assemblies share the modular architecture of the 16-mer (Fig. 3a,b). In all three cases, the tetramers have the same curvature. The ACD positions within the tetramers are identical. In the apical regions of 12- and 20-mers, the CTRs do not swap domains due to the large distance between adjacent protomers, as for the 16-mer. However, the CTRs of all M_{eq} are in the non-3D domain-swapped state in the 12-mer, while those of the 20-mer connect neighboring tetramers by domain-swapping (Fig. 3). As estimated from the relative abundances of all subpopulations, ~20% of all CTRs are in the 3D domain-swapped state in the ensemble subset studied (Supplementary Table 1). Domain-swapping of the CTR, as suggested by cryo-EM, would require large-amplitude motions of the polypeptide chain also in the hinge region (I146-E156) adjacent to the ACD. The CTR of αA-crystallin displays significant flexibility and can be detected by solution-state NMR (residues G149-S173, Fig. 3c)[28]. To test the prevalence of 3D domain-swapping of the CTR in the reduced αA-crystallin ensemble, we performed paramagnetic relaxation enhancement (PRE) experiments on αA_{red} labeled with 3-(2-iodoacetamido)-proxyl spin label (IPSL) at the cysteine residues within the ACD (most likely C142). The spectra of the spin-labeled ^{15}N-αA_{red} sample (^{15}N-αA_{red}-IPSL) showed a substantial decrease (~40-50%) of the peak intensity ratios between the paramagnetic (IPSL oxidized) and diamagnetic (IPSL reduced) states (I_{para}/I_{dia}) for residues in the IPV region, such as A158, I159 and V161 (Fig. 3e).

If the observed PREs were a consequence of random-coil-like structural fluctuations of the CTR, PRE effects would localize around C142 (± 10 amino acids)[44]. We observe, however, a flat PRE profile with minimum intensity around A158, suggesting that the CTR is either partially structured or exchanges between a bound and a free form. We can exclude the former interpretation as the CTR chemical shifts of IPSL-oxidized and IPSL-reduced spin-labeled αA-crystallin are rather similar (Extended Data Fig. 6).

Due to the high molecular weight of the αA-crystallin oligomers, no direct PREs can be measured for the CTR-bound state. However, chemical exchange between bound and unbound CTRs allows indirect access to assess the proximity of the CTR to the β4/β8 groove[45]. The measured transfer-PREs thus allow us to probe intra- and intermolecular 3D domain-swapping.

To distinguish whether the unbound CTRs are in proximity of the ACD of the same protomer (non-3D domain-swapped) or an adjacent one (3D domain-swapped), we incubated spin-labeled ^{14}N-αA$_{red}$ (^{14}N-αA$_{red}$-IPSL) with ^{15}N-αA$_{red}$ in a 1:1 molar ratio (^{15}N-αA$_{red}$+^{14}N-αA$_{red}$-IPSL). In the case where all CTR interactions involve 3D domain-swapping, an attenuation of the signal intensity by 25% would be expected. The fact that only a decrease by 10-15% in the peak intensity is observed (Fig. 3f) is in agreement with the cryo-EM results, which indicate ~20% of the CTRs to be in a 3D domain-swapped state (Supplementary Table 1). Both experiments thus imply that the 3D domain-swapped state is not dominantly populated in the oligomer ensemble of αA$_{red}$.

In vitro formation of an intramolecular disulfide bond in human αA-crystallin

In agreement with the literature[32,33], we detected in an Ellman's assay of αA$_{red}$ 0.93 ± 0.008 mol (SH) / mol (protein) corresponding to one accessible cysteine residue *in vitro*. The presence of only one reactive cysteine is puzzling at first glance, considering that the cysteines C131 and C142 of human αA-crystallin form an intramolecular disulfide bridge *in vivo* [34–37]. However, when performed in the presence of urea, the Ellman's assay detected 1.92 ± 0.070 mol (SH) / mol (protein) for αA$_{red}$. Thus, the second cysteine is not readily accessible under native conditions.

In our pseudoatomic model of αA$_{red}$, the cysteines are located on the adjacent antiparallel β8- and β9-strands and point in opposite directions (Fig. 3d). Their C$_α$ atoms are ~6 Å apart, which is within the Cα-Cα distance range of 3.8-6.8 Å usually observed for disulfide bond conformations in proteins, but farther than the mean Cα-Cα distance of ~4.6 Å found in cross-strand disulfides[46]. The formation of a cross-strand disulfide bond between C131 and C142 would require rotation of the cysteine side chains towards each other, resulting in significant conformational changes upon oxidation of αA-crystallin.

To study the formation of an intramolecular disulfide bond we performed redox titrations with glutathione (Fig. 4). At -149 mV, roughly 50% of the protein was oxidized to the intramolecularly cross-linked species (αA$_{ox}$), while the remaining fraction consisted of intermolecularly disulfide-linked dimers (~20%) and trimers (~14%) (Fig. 4a). Upon quantification of the ratio of αA$_{red}$ and αA$_{ox}$ monomer bands, the equilibrium constant of the redox reaction for intramolecular disulfide bond formation, K_{eq}, was determined to be 0.434 mM corresponding to a redox potential of the intramolecular disulfide of -135 mV (Fig. 4c).

For comparison, the above value is between the redox potentials of the catalytic disulfides in bacterial DsbA and DsbC, oxido-reductases with a strained conformation in the oxidized state[47,48]. The low reaction rate and the formation of a substantial amount of intermolecularly disulfide-bridged species suggest a thermodynamically unfavorable

conformational state for intramolecular disulfide formation also in the case of αA-crystallin. Thus, a denaturant should facilitate oxidation. Indeed, in the presence of urea, the disulfide-linked oligomers were abolished and half-maximal oxidation was achieved at -222 mV (Fig. 4d,f), again implying that destabilization leads to the accessibility of both cysteines. As a consequence, we prepared αA_{ox} by incubation with GSSG in the presence of urea. According to Ellman's assays this preparation contains no free sulfhydryls: -0.03 ± 0.037 mol (SH) / mol (protein). We also performed the titration reactions with $\alpha A_{ox.}$ (Fig. 4b,e). The results indicated that after 20 h, the forward and reverse reactions were indistinguishable and the thermodynamic equilibrium attained (Fig, 4c,f).

Structural impact of the intramolecular disulfide bond on human αA-crystallin

Circular dichroism (CD) spectroscopy showed that oxidation does not lead to pronounced changes in the secondary structure (Extended Data Fig. 7a). However, differences became apparent in the environment of phenylalanine, tyrosine and tryptophan residues (Extended Data Fig. 7b). Given that ~60% of the Phe and Tyr residues, as well as the single Trp, are located within the NTR, altered tertiary interactions within the NTR upon oxidation appear likely.

Electron micrographs of negatively stained αA_{ox} revealed that the protein assembles into oligomers that are more polydisperse and larger than observed for αA_{red} (Fig. 5a). The average oligomer size shifted from ~13.5 nm for αA_{red} to ~17.7 nm for αA_{ox} (Fig. 5b). In agreement, size exclusion chromatography (SEC) experiments indicated an increase in molecular mass from 380 kDa for αA_{red} to 770 kDa for αA_{ox} (Extended Data Fig. 7c) and sedimentation velocity analytical ultracentrifugation (aUC) experiments showed an increase in the sedimentation coefficient ($s_{20,w}$)[19] from 14 S to 25 S (Extended Data Fig. 7d).

The projections seen in electron micrographs of negatively stained αA_{ox} particles were either round or slightly elongated (Fig. 5a) and resembled projections seen in αA_{red} samples. A preliminary 3D reconstruction of a 32-mer calculated from class averages of 1,500 single-particle images (Extended Data Fig. 7e), without employing any starting model, revealed a hollow, slightly elongated assembly with D2 symmetry (Fig. 5c and Extended Data Fig. 7f). Notably, the assembly contains the characteristic Z-shaped tetramers as seen in the oligomers of αA_{red} (Fig. 1), but it is expanded through the insertion of further building blocks apparently composed of dimers (Fig. 5c).

The overall architecture of the αA_{ox} 32-mer implies altered residue and/or subunit proximities and consequently an altered cross-linking behavior compared to αA_{red}. Due to the lack of quantitative cross-linking data, we only tentatively compared both patterns in their most striking features. This comparison revealed a higher number of interactions in αA_{ox} (Supplementary Table 3), which included those observed for αA_{red} but also indicated differences between the two redox states. As such, many cross-links observed only in αA_{ox} involved residues located within the NTR as well as within the β4-, β6+7- and β9-strands (including K145), suggesting alteration of their relative positions and/or enhanced side chain accessibilities in αA_{ox} (Extended Data Fig. 4b).

The intramolecular disulfide affects local structural dynamics of αA-crystallin

To further test how intramolecular disulfide formation affects the structure and dynamics of αA-crystallin, we performed hydrogen-deuterium exchange coupled to mass spectrometry (H/DX-MS) (Fig. 6a and Supplementary Fig. 1). In agreement with previous studies[49], peptides from the NTR were characterized by a moderate protection at short D_2O exposure times, but became increasingly deuterated at longer exposure, consistent with the dynamic nature of this region sampling different conformations. The peptides from the ACD showed in general lower exchange. The β5- and β6+7-strands (F93-E102 and Y109-R119, respectively) were most strongly protected, while the CTR exchanged readily, consistent with high accessibility/flexibility. Thus, the degree of exchange in αA_{ox} was similar to that observed for αA_{red}, but specific differences existed. In αA_{ox}, the N-terminal stretch comprising residues D2-F10 exhibited increased protection. The β6+7-strand (Y109-R119), the C-terminal region of the β8-strand (L133 and S134) and the β9-strand (L139-G143), as well as the loop connecting the latter, became deprotected upon disulfide formation, with F141 (β9-strand, neighboring C142) showing the strongest deprotection. These results suggest that the introduction of the intramolecular disulfide affects dynamics, solvent exposure and the hydrogen bonding network around the sites of disulfide formation (Fig. 6b).

To test oligomer stability, we performed aUC experiments in the presence of urea. With increasing urea concentrations, both αA_{red} and αA_{ox} oligomers dissociated successively. A dissociated species with a sedimentation coefficient of ~2 S was observed at 4.5 M urea for αA_{red} and at 3.5 M urea for αA_{ox} (Extended Data Fig. 8a). Similarly, urea-induced unfolding transitions monitored by intrinsic fluorescence revealed cooperative unfolding with midpoints at 3.8 and 2.7 M urea for αA_{red} and αA_{ox}, respectively (Extended Data Fig. 8b).

Chaperone activity of oxidized αA-crystallin

To compare αA_{red} and αA_{ox} functionally, we performed *in vitro* aggregation assays using the cellular tumor antigen p53 (p53) and malate dehydrogenase (MDH) as model substrates and assessed the redox states of αA-crystallin and the substrate. For comparison, we performed the same experiments in the presence of GSSG and the reduced and oxidized forms of DsbA ($DsbA_{red}$ and $DsbA_{ox}$, respectively). The heat-induced aggregation of p53 was efficiently suppressed only in the presence of αA_{ox} (Fig. 7a). Remarkably, when αA_{ox} was present, disulfide-linked large oligomers of p53 were formed early and concomitantly αA_{red} appeared (Fig. 7b), indicating that the disulfide in αA_{ox} was transferred to p53. When we added $DsbA_{ox}$, only a slight aggregation suppression activity was detected (Fig. 7a). However, also in this case, high molecular weight disulfide-bonded p53 aggregates were formed (Fig. 7b) at a rate similar to that observed for αA_{ox} (Fig. 7c). These results indicate that αA_{ox} and $DsbA_{ox}$ share the ability to transfer their disulfide bond to destabilized p53. The addition of GSSG neither suppressed aggregation nor led to the early formation of disulfide-linked species (Fig. 7a,b). Such species were also absent when αA_{red} or $DsbA_{red}$ was present (Extended Data Fig. 9a).

Both αA_{red} and αA_{ox} suppressed the heat-induced aggregation of MDH (Extended Data Fig. 9b). As in the case of p53, αA_{ox} transferred its intramolecular disulfide almost quantitatively to MDH, resulting in intermolecularly cross-linked MDH species (Extended Data Fig. 9c,d). In the presence of $DsbA_{ox}$, the MDH monomer band disappeared (Extended Data Fig. 9c), but disulfide-bonded oligomers were not detected, possibly due to their large size (Extended Data Fig. 9d). In the presence of GSSG or $DsbA_{red}$, the aggregation kinetics of MDH was similar to the control, and no cross-linked MDH species were observed (Extended Data Fig. 9b,d,e).

Taken together, the above results demonstrate that αA_{red} and αA_{ox} differ in their *in vitro* chaperone activities towards model substrates, and αA_{ox}, similar to DsbA, is capable of transferring its disulfide bond to destabilized model substrates.

Discussion

Human αA-crystallin exists in heterogeneous ensembles of oligomers of varying subunit stoichiometries. The atomic models determined by combining data from cryo-EM, X-ray crystallography, cross-linking/mass spectrometry, NMR and molecular modeling reveal the roles of the NTR and CTR in oligomerization and C-terminal domain-swapping as a determinant of ensemble heterogeneity. The recurring unit of αA_{red} oligomers is a tetramer in which two β7-interface dimers associate at the equator of the barrel-shaped assembly through N-terminal interactions. Further N-terminal interactions at the poles mediate the formation of higher-order assemblies by linking tetrameric units. A tetrameric building block is consistent with previous studies[20–23].

The homology-modeled structure of the NTR contains three short helices connected by flexible loops, consistent with the propensity of NTRs to adopt secondary structure elements[29,50]. These regions are highly dynamic and exist as ensembles of heterogeneous conformations[29,51,52]. In αA-crystallin, even the protomers in the apical and equatorial regions of the same oligomer possess different conformations. In our model, representing one of several possibilities, the N-terminal interactions occur mainly between the loops connecting helices α2 and α3. The amphipathic helix α2 (residues 20-27) covering the conserved phenylalanine-rich sequence RLFDQXFG[14] dictates the position of the interacting loop regions in equatorial protomers. This motif was implicated in contributing to the higher order subunit assembly, oligomer stability and dynamics[53].

The CTR of αA_{red} occurs in non-3D and 3D domain-swapped configurations, as previously captured in crystals of truncated forms of zebrafish [16] and bovine αA-crystallin [15], respectively. We show that both configurations coexist in solution. The transition between the two states requires the dissociation of the IPV motif from the β4/β8 groove. However, NMR studies on human αB-crystallin[54] and Hsp27[55] show that the IXI motif is highly dynamic in solution and not rigidly bound to the protein scaffold. In αA-crystallin, the enhanced dynamics of the CTR are likely to facilitate domain-swapping.

In human αA-crystallin, the interplay between the geometric constraints imposed by the assembly architecture and the hinge loop connecting the CTR to the ACD is likely to dictate

the propensity for domain-swapping. In all three assemblies, distance constraints preclude intermolecular binding of the CTR in apical protomers. Our reconstructions are of similar dimensions but differ in their number of subunits, leading to closer packing of protomers; i.e. equatorial inter-protomer distances decrease gradually from 12-mer to 20-mer. Consequently, in equatorial protomers of the 12-mer, the non-3D domain-swapped configuration is favored, as a flexible chain of a given length is less likely to span large distances relative to its own length, resulting in folding back of the chain on itself (non-3D domain-swapped configuration). Shorter distances promote domain-swapping in all equatorial protomers of the 20-mer population. In the 16-mer population, both configurations coexist; nevertheless, the 3D domain-swapped state might impose more strain on the hinge region, and is thus less favored.

Despite the high similarity at the sequence level and virtually the same monomer length, αA- and αB-crystallin form different geometric bodies utilizing the same type of interactions: the β7-interface mediates dimerization and oligomerization is supported by N-terminal interactions, as well as by IXI-binding to the neighboring protomer. While the CTR is decisive in the formation of hexameric species of human αB-crystallin[56,57], the CTR of human αA-crystallin contributes to the formation of higher-order oligomers only in the 3D domain-swapped form. N-terminal interactions are key to oligomer formation for all assembly types: the 12-meric species, the most abundant oligomer population, assembles without participation of the CTR in intermolecular interactions, indicating that there is no stringent contribution of the IXI motif to oligomer formation. Consistent with this, both human[58] and bovine[59] αA-crystallin retain their ability to oligomerize upon mutation of the IXI motif or its deletion[24].

αA_{ox} is highly abundant in young lenses without interfering with lens transparency[36]. The oxidation of αA-crystallin *in vitro* requires the presence of destabilizing agents which leads to the dissociation of oligomers. This suggests that local conformational changes and/or partial unfolding occur, putting the two cysteines in the β8- and β9-strands in an appropriate spatial proximity. It has been suggested that partial unfolding of monomers upon dissociation may be a common property of human sHsps and partly unfolded monomers may exist within larger oligomers[60,61]. Upon removal of urea, αA_{ox} reassembles into oligomers that are distinct from those of αA_{red} harboring subunits, which are locally more dynamic in their β6+7-, β8- and β9-strands.

The redox potential of the intramolecular disulfide bridge in human αA-crystallin is comparable to that determined for thiol-disulfide oxido-reductases[47,62]. In the presence of urea, the intramolecular disulfide is formed at -220 mV, which is even below the estimated redox potentials of approximately -204 mV and -217 mV at the nuclear and cortical regions, respectively, of the young lens[63,64], thus enabling the formation of the intramolecular disulfide bridge *in vivo*, for an unfolded or destabilized chain. Although it is delicate to deduce the redox potential of a disulfide bond *in vivo* from the redox potential determined *in vitro* under equilibrium conditions in dilute solutions, the mere existence of the intramolecular disulfide in αA-crystallin *in vivo* hints at certain similarities of its redox properties *in vitro* and *in vivo*.

The intramolecular disulfide bridge in human αA-crystallin is a cross-strand disulfide. Such disulfides are often reactive redox-based conformational switches due to their strained conformation[65]. Although the edge strand β8 might tolerate the conformational changes/distortions caused by the disulfide bond to a certain extent, the diminished stability of αA_{ox} against urea-induced dissociation and unfolding compared to αA_{red} supports a strained structure.

Interestingly, the two cysteines in human αA-crystallin are conserved among primates. *In vivo*, introduction of additional cysteine residues may be detrimental, as naturally occurring arginine to cysteine mutations of human αA-crystallin are associated with cataract[5]. Together with the general evolutionary selection against cysteines, this suggests that the cysteines of human αA-crystallin must serve a function in the eye lens. This notion appears contradictory to the increase of intramolecular disulfides concomitant with a decrease in chaperone activity of αA-crystallin during aging and cataractogenesis[42]. It should, however, be noted that mere coincidence of these processes has been demonstrated, but not a direct causality. The precise relationship between cysteine oxidation and cataractogenesis needs to be further clarified.

αA_{ox} is able to transfer its intramolecular disulfide to destabilized substrates; it has redox properties intermediate between disulfide oxidases DsbA and DsbC. Given that it constitutes roughly ~15-20% of the eye lens proteins, this corresponds to an intracellular concentration of 3-4 mM. The lenticular glutathione concentration is on the order of ~3.7 mM in the outer cortical regions and ~2.8 mM in the nuclear regions of young lenses[64,66]. It is therefore likely that the redox state of the eye lens is not solely dictated by the glutathione system, but αA-crystallin itself will be an integral co-determinant of the lenticular redox system and a yet unknown player in lenticular redox homeostasis. It could well be that the preferential oxidation of αA-crystallin prevents the formation of non-native disulfide bonds in other crystallins and thus their aggregation in the eye lens. Further *in vivo* studies are required to address this issue.

Taken together, our structural analysis of αA-crystallin revealing the assembly principles of its oligomer ensembles, together with the properties αA_{red} and αA_{ox}, provides a framework for understanding its role in the normal lens and in cataractogenesis.

Online Methods

Cloning and protein purification

Wild-type human αA-crystallin was recombinantly produced in *E. coli* at 20°C. The cells were harvested by centrifugation and disrupted in the presence of protease inhibitor mix G (Serva, Heidelberg, Germany). The first purification step was anion exchange chromatography (Q-Sepharose FF). After fraction pooling, urea was added to 4.5 M final concentration, then cation exchange (SP-Sepharose FF) and gel filtration chromatography (Superdex 75) were performed. After an additional high-resolution anion exchange chromatography step, urea was removed by dialysis against PBS (137 mM NaCl, 2.7 mM KCl, 8.1 mM Na_2HPO_4, 1.76 mM KH_2PO_4, pH 7.4), 1 mM EDTA, 1 mM DTT. As a final polishing step, a gel filtration run (Superdex 200; PBS, 1 mM EDTA, 1 mM DTT) was

performed, yielding αA_{red} preparations of > 95% homogeneity as judged by SDS-PAGE. Aliquots were stored at -80 °C in gel filtration buffer. Before all experiments, protein aliquots were thawed and incubated for 3 h at 37 °C to ensure proper thermal equilibration. If not stated otherwise, all experiments were performed in PBS buffer, 1mM EDTA, with either 1 mM DTT or 1 mM *trans*-4,5-dihydroxy-1,2-dithiane (DTT_{ox}) present. For experiments in which reductants or oxidants were likely to interfere, the buffer was exchanged to thoroughly degassed and N_2-purged PBS, 1 mM EDTA using 7K MWCO polyacrylamide desalting columns (Thermo Scientific, Waltham, MA, USA) to remove residual DTT. Further experimental details are described in Supplementary Note 1.

Redox titration, preparative protein oxidation and Ellman's assay

Redox titrations were performed according to Wunderlich & Glockshuber[47]. To rule out potential interference of O_2 from air during redox titrations, the water used for the preparation of buffer was thoroughly degassed and purged with N_2 over night. Pipetting steps and incubation for equilibration were carried out in an anaerobic chamber (Coy laboratory products, Grass Lake, MI, USA) under a N_2/H_2 (98%/2%) atmosphere. All solutions were transferred into the anaerobic chamber immediately after preparation in N_2-purged water. All reagents and tubes were stored in the anaerobic chamber at least 24 h before the start of the experiment. Initially, the storage buffer of αA_{red} was exchanged to PBS, 1 mM EDTA using gel filtration spin columns, the protein was transferred to the anaerobic chamber and diluted (10 μM final concentration) into buffers of a specified redox-potential as defined by a mixture of oxidized and reduced glutathione, GSSG and GSH, respectively, in PBS, 1 mM EDTA. The total concentration of glutathione monomers was kept at 5 mM for all reactions. After equilibration for 20 h at 43 °C, disulfide exchange was quenched by the addition of 25 mM *N*-ethyl-maleimide (NEM, dissolved in dry ethanol) and incubation for 20 min at 20°C. For redox-titrations in the presence of urea, all redox buffers and the buffer for initial DTT removal contained 4.5 M urea. The quenched reactions were analyzed by loading 1 μg of total protein per lane onto gradient gels (TG Prime, 8-16%, Serva, Heidelberg, Germany), using non-reducing sample buffer. The relative amount of remnant reduced and oxidized monomeric αA-crystallin (fraction oxidized, O) was quantified by densitometry using ImageJ. The equilibrium constant for the formation of the intramolecular disulfide K_{eq} was determined through nonlinear regression of the data using the function $O = 1 - ([GSH]^2/[GSSG])/(K_{eq} + [GSH]^2/[GSSG])$. The K_{eq} values obtained (4.3×10^{-4} M for the reaction of αA_{red} under native conditions and 9.2×10^{-4} M for αA_{ox} under native conditions, 0.257 M for the reaction of αA_{red} in the presence of urea and 0.306 M of αA_{ox} in the presence of urea) were used to determine the corresponding redox potential at 43 °C and pH 7.4 from the Nernst equation $E_{0\ \alpha A} = E_{0\ GSH/GSSG} - (RT/nF) \times \ln K_{eq}$ with $E_{0\ GSH/GSSG} = -240\ mV$, which is the standard potential for the glutathione redox pair at 40 °C and pH 7.4[67]. To assess the reversibility of the reaction, the titrations were equivalently performed using αA_{ox}. The data for αA_{ox} were processed as for αA_{red}.

To produce preparative amounts of αA_{ox}, αA_{red} at a concentration of 50 μM was subjected to buffer exchange using a HiPrep 26/10 desalting column (GE Healthcare) equilibrated in PBS, 1 mM EDTA, 4.5 M urea. Subsequently, the eluting protein was brought to 37 °C, supplemented with 2.5 mM GSSG and 5 μM GSH, and incubated for 6 h at 37 °C. After

incubation, the redox system was removed by exchanging the buffer to PBS, 1 mM EDTA, 4.5 M urea. The eluate was then dialyzed twice against 5 L of PBS, 1 mM EDTA. The oxidation state of the protein was validated after quenching with NEM by non-reducing SDS-PAGE.

The Ellman's assay was performed according to Simpson, 2008[68]. The reaction was scaled to 100 µL volume and the final protein concentrations in the reaction mixture were 26 µM for αA_{red} and 22 µM for αA_{ox}.

Quaternary structure analysis

The quaternary structure of αA-crystallin samples was determined by analytical gel filtration (SEC), analytical ultracentrifugation (aUC) and negative stain electron microscopy (NS-EM). SEC runs were performed on a Superose 6 10/300 GL (GE Healthcare, Chalfont St Giles, UK) column using absorbance detection. For aUC, sedimentation velocity experiments were carried out on a ProteomeLab XL-I analytical ultracentrifuge (Beckman Coulter, Brea, CA, USA) at 20 °C. Protein was detected by UV absorbance. For urea titration aUC experiments, αA-crystallin stock solution was diluted to 20 µM in buffer containing the indicated concentrations of urea. The solution was allowed to equilibrate at 20 °C for 5 h. The sedimentation velocity profiles were analyzed with the dc/dt method[69] and extrapolated to 20 °C and water as a solvent, giving the $s_{(20,w)}$. Negative staining experiments were conducted as described previously[19]. Oligomer sizes were determined as diameters of circumscribing circles of the class averages using ImageJ (version 1.47t). Further experimental details are described in Supplementary Note 1.

Extrinsic and intrinsic fluorescence and circular dichroism (CD) spectroscopy

To assess protein stability, urea-induced unfolding equilibria were determined as a function of the urea concentration by intrinsic fluorescence measurements. Unfolding mixtures contained 4 µM of protein and the indicated amount of urea dissolved in degassed, N_2-purged PBS, 1 mM EDTA with 1 mM DTT or DTT_{ox}. The concentration of urea was verified by refractive index determination. Samples were incubated for 16 h. Spectra were measured in triplicates using a Jasco FP-6500 spectrofluorimeter (Jasco, Tokyo, Japan) connected to a thermostat. Hellma QS 10mm x 2 mm fluorescence ultra-micro cuvettes (Hellma, Müllheim, Germany) were used for fluorescence measurements. The excitation wavelength was set to 295 nm and emission spectra were recorded from 305 nm to 450 nm. During incubation and measurement, the samples were kept at 20 °C. The acquired spectra were corrected for the corresponding buffer signal. For each spectrum, at a given concentration of urea (denoted as [urea]), the intensity averaged emission wavelength $\langle\lambda\rangle_{[urea]}$ was calculated[70]. The fraction of natively folded protein (f_{folded}) was calculated for the measurement range between 0 M urea and 7.5 M urea as $f_{folded} = \langle\lambda\rangle_{(7.5M\ urea)} - \langle\lambda\rangle_{[urea]} / \langle\lambda\rangle_{(7.5M\ urea)} - \langle\lambda\rangle_{(0M\ urea)}$ and plotted versus denaturant concentration.

Circular dichroism (CD) spectra in the near (250-320 nm) and far (180-260 nm) UV-range were measured using a Jasco J-710 (Jasco, Tokyo, Japan) or a Chirascan (Applied Phostophysics, Leatherhead, United Kingdom) circular dichroism spectrophotometer equipped with a thermostated cuvette holder set to 20 °C. Near-UV CD spectra were

recorded at a protein concentration of 100 μM, far-UV CD spectra were measured at 40 μM in 20 mM KH_2PO_4/KOH, pH 7.4, 1 mM EDTA. To record near-UV spectra, a QS 1 cm cuvette was used and for far-UV spectra a detachable window QS 0.2 mm cuvette (both Hellma, Müllheim, Germany).

Hydrogen/deuterium exchange–mass spectrometry

H/DX-MS experiments were performed using an ACQUITY UPLC M-class system with H/DX technology (Waters, Milford, MA, USA). H/DX kinetics were determined by measuring data points at 0, 10, 60, 600, 1,800 and 7,200 s exposure to deuterated buffer at 25 °C. At each data point, 4 μL of a solution of 30 μM protein was diluted automatically 1:20 into PBS, 1 mM EDTA, 1 mM DTT or 1mM *trans*-4,5-dihydroxy-1,2-dithiane, pD 7.5, prepared with 99.9% D_2O or H_2O as reference buffer. The reaction mixture was quenched by the addition of 200 mM KH_2PO_4, 200 mM Na_2HPO_4, 4 M GdnHCl, 300 mM TCEP, pH 2.3 (titrated with HCl) in a ratio of 1:1 at 0 °C. A 50 μL volume of the resulting sample was subjected to on-column peptic digest on an in-line Enzymate BEH pepsin column (2.1 x 30 mm) at 20°C. Peptides were trapped and desalted by reverse phase chromatography at 0° C using an Acquity UPLC C18 BEH VanGuard pre-column (1.7 μm C18 beads, 2.1 x 5 mm, Waters). For separation, an Acquity UPLC BEH C18 (1.7 μm, 1 x 100 mm) analytical column (Waters) was used at 0° C, using gradients with stepwise increasing acetonitrile (in 0.1% formic acid) concentration from 5 to 35% in 6 min, from 35 to 40% in 1 min and from 40 to 95% in 1 min. The eluted peptides were analyzed using an in-line Synapt G2-Si QTOF HDMS mass spectrometer (Waters). MS data were collected over an m/z range of 100-2000. Mass accuracy was ensured by calibration with [Glu1]-Fibrinopeptide B (Waters) and peptides were identified by triplicate MS^E, ramping the collision energy from 20 to 50 V. Data were analyzed using the ProteinLynx Global Server (PLGS, Version 3.0.3) and DynamX (Version 3.0) software packages (Waters). As all samples were handled under identical conditions, deuterium levels were not corrected for back-exchange and were therefore reported as relative deuterium uptake levels. Briefly, for each peptide, the relative fractional exchange is calculated dividing the deuterium level incorporated at a given timepoint (in Da) by the total number of backbone amide hydrogens in the peptide (this equals the number of amino acids, minus proline residues minus 1 for the N-terminal amide[71]). All experiments were performed with triplicate determination at each time point.

Aggregation assays

Chaperone assays and disulfide-transfer reactions were performed in parallel using malate dehydrogenase (MDH) or human p53 (p53) as model substrates in the absence of reductant. MDH was diluted to 4 μM and p53 was diluted to 2 μM into PBS containing 1 mM EDTA on ice. Oxidized and reduced αA-crystallin, oxidized and reduced DsbA and GSSG were added to a final concentration of 4 μM. The reaction mix was split in two aliquots. One of the aliquots was used to follow the aggregation of model substrates at 45 °C by recording the absorbance at 360 nm for 60-120 min using a Cary 50 UV/VIS spectrophotometer (Varian, Palo Alto, CA, USA) equipped with a temperature-adjustable cuvette holder. The other aliquot was used to withdraw samples at the indicated timepoints. One sample was withdrawn at t = 0 min for reference before starting the reaction by placement of the reaction mixtures to 45 °C in the photometer. The disulfide exchange reaction in every sample was

Europe PMC Funders Author Manuscripts

quenched immediately after withdrawal by the addition of NEM dissolved in dry ethanol to 25 mM final concentration. After 20 min of incubation at 20 °C, non-reducing SDS-PAGE sample buffer was added, the sample was incubated at 95°C for 5 min and analyzed on an 8-16% gradient gel (TG Prime, Serva, Heidelberg, Germany).

Cryo-electron microscopy, image processing and 3D-reconstruction

Sample preparation, data collection—For the preparation of the cryo-EM samples, 4 μL of αA_{red} solution (0.3 mg/mL in PBS, 1 mM EDTA, 1 mM DTT, pH 7.4) were applied to glow-discharged Quantifoil R 2/1 holey carbon copper grids, incubated for 30 s, blotted and plunge-frozen in liquid ethane using a manual plunger. The samples were mounted into autoloader cartridges and transferred into a Titan Krios electron microscope (FEI, Hillsboro, OR, USA) equipped with a K2 Summit direct detector (Gatan, Pleasanton, CA, USA) and operated in energy-filtered transmission electron microscopy (EFTEM) mode at 300 kV. Automatic data acquisition was performed using the TOM toolbox[72]. 2,334 movie images were collected at defocus values ranging from -1.2 μm to -2.5 μm and at a nominal magnification of ×37,000 (1.35 Å per pixel) in 'super-resolution mode' (0.675 Å per pixel). The movies were recorded at dose rates of 7-8 electrons per pixel per second, with exposure times of 0.37-0.27 s per frame and a target total dose of 25-36 electrons per $Å^2$. The frames were aligned, averaged and binned to a final pixel size of 1.35 Å per pixel. Well-separated particle images were selected manually and extracted into 200×200 pixel boxes using 'e2boxer' of the EMAN2 software package[73]. Images were corrected for the contrast transfer function by phase flipping using Bsoft[74]. All subsequent image processing procedures were carried out within the IMAGIC5 suite[75].

Image processing and 3D-reconstruction—For the processing of the cryo-EM data, reference-free class averages were generated from 74,068 CTF-corrected and bandpass-filtered (20-160 Å) single-particle images. The class averages revealed almost spherical particles ranging in size between 6 and 16 nm, as well as elongated ones with a maximum length of 14 nm. The presence of 2-, 3-, 4- and 5-fold symmetries in projection images together with the variation of particle dimensions and shapes suggested the presence of multiple structures of a similar barrel-like architecture but of varying subunit stoichiometries. Based on this, three models, each consisting of a bundle of 'pillars' (3, 4 and 5 pillars, compatible with 3-, 4- and 5-fold symmetries) were generated as starting references. Reference-free class averages were sorted into initial particle subsets based on particle diameter and symmetry. Within each subset, an initial 3D-reconstruction was calculated by projection matching cycles using the above 'pillar-bundle' models as starting models. In a next step of data sorting, the three initial 3D-reconstructions were used as references to align and sort all single-particle images of the cryo-EM data set into three final subsets in an iterative procedure. All particles were aligned independently by multi-reference alignment (MRA) to each of the three reference structures. Within each of the three particle sets, multivariate statistical analysis (MSA) was applied to generate class averages. The Euler angles of the class averages were assigned by angular reconstitution (AR)[76]. Subsequently, classes that mismatched with the corresponding model reprojections were sorted out. This 'purification' step by MSA/AR was repeated until all remaining class averages agreed well with reference reprojections, resulting in three distinct particle subsets.

For 3D-reconstruction, the final class averages were refined iteratively by six rounds of MRA and AR using starting models generated from the input class averages of the respective set. For the refinement, single-particle images of each class were aligned with the corresponding reprojection of the respective preliminary reference, while particles that were rotated by more than 9° as well as the 10% of images with the lowest cross-correlation coefficients were ignored. Euler angles of the class averages comprising the remaining particles were refined by AR and a new 3D-reconstruction was calculated, which served as a reference for the subsequent refinement cycle. During refinement, filtering of input and output images as well of the reference models changed in every iteration starting from 20 Å and ending at 7 Å to sequentially allow more details to affect the alignment. Class averages and 3D-reconstructions were masked with an adaptive soft edge mask unless when used for Fourier shell correlation (FSC) calculations.

For resolution determination, the ‘gold standard’ 0.143 criterion was used[77]. FSCs were calculated between the final reconstructions of independently processed half sets using the FSC validation server (http://pdbe.org/fsc) within the PDBe (Protein Data Bank in Europe)[78]. 3D reconstructions and atomic models were rendered using UCSF Chimera[79].

3D sampling and classification—To analyze the conformational heterogeneity of human αA-crystallin oligomers, the particles from the final oligomer subsets were subjected to bandpass filtering (140-10 Å), normalization and 3D sampling[80], followed by 3D classification. Within each dataset, 1,000 random 3D-reconstructions from randomly selected 1,000 projection images were generated (3D sampling of structure subensembles). The 3D-reconstructions were analyzed by 3D MSA followed by clustering into 10 distinct subpopulations by 3D-classification using IMAGIC5[75].

NMR spectroscopy

αA_{red} was $^{15}N/^{13}C$-labeled upon recombinant expression and purified as described above. Purified protein was dialyzed against 10 mM HEPES/KOH (pH 7.4), 2 mM DTT, 1 mM EDTA. Solution-state NMR experiments were carried out employing a Bruker Biospin Avance III spectrometer operating at a ^{1}H Larmor frequency of 950 MHz (22.3 T) using a CPTCI triple-resonance cryoprobe. All experiments were performed at 300 K in HEPES/KOH buffer containing 5% D_2O. For spin-labeling experiments, 3-(2-iodoacetamido)-proxyl (IPSL, Sigma-Aldrich, St. Louis, MO, USA; 50 mM stock dissolved in DMSO) was used. As only one cysteine residue is readily surface accessible in native αA-crystallin, the label was most likely reacted with C142[32,33]. As a control, protein-bound IPSL was reduced with a 10 molar excess of freshly prepared ascorbic acid in HEPES/KOH buffer to yield the diamagnetic species. Paramagnetic relaxation enhancements (PREs) arising from the spin label were determined using the ratio of peak intensities of the ^{1}H, ^{15}N-HSQC spectra obtained for the paramagnetic (oxidized) and the diamagnetic (reduced) state (I_{para}/I_{dia}), in the absence and presence of 10 molar equivalents of ascorbic acid. Further experimental details are described in Supplementary Note 1.

Cross-linking and mass spectrometry

For cross-linking experiments, bis(sulfosuccinimidyl)suberate (BS3) cross-linker (Thermo Scientific, Waltham, MA, USA) was added to the protein upon continuous vortexing of the protein solution. The reaction mixture was incubated at 20 °C for 1 h and quenched. The samples were loaded on gradient gels, which were run at a constant voltage of 200 V using MOPS-SDS -running buffer. The protein in excised gel bands was alkylated with iodoacetamide (IAA) and digested with trypsin (Thermo Fischer Scientific), following previously established protocols[81]. Peptides were separated by reverse-phase chromatography and analysed by LC-MS/MS on an Orbitrap Fusion Lumos (Thermo Fisher Scientific) with a 'high/high' acquisition strategy. The mass spectrometric raw files were processed into peak lists using MaxQuant (version 1.5.3.30)[82], and cross-linked peptides were matched to spectra using Xi software (version 1.6.745)[83]. FDR was estimated using XiFDR on 5% residue level[84]. Further experimental details are described in Supplementary Note 1.

Model building

Structural modeling of the human αA-crystallin 16-mer was based on homology models of either the non-3D domain-swapped structure of truncated αA-crystallin ($\alpha A_{60–166}$) from zebrafish (PDB 3N3E) [16] or on the 3D domain-swapped structure of bovine truncated αA-crystallin (αA_{59-163}) (PDB 3L1E)[15] using the program Modeller[85]. The N-terminal segment ($\alpha A_{1–59}$) was modeled using I-Tasser[86]. Homology modeled ACD dimer structures were fitted as rigid bodies into the corresponding cryo-EM densities using the program colores of the Situs package[87]. The N-terminal modeled segment ($\alpha A_{1–59}$) was placed randomly in various positions. The oligomers were energy minimized using the Sander module of the Amber software package (Amber16)[88]. Molecular dynamics (MD) flexible fitting was started from energy-minimized structures using the emap option in Sander[89]. For each of the initial placements of the N-terminal segments, the final flexibly fitted structure was evaluated based on RMSD, stereochemistry and cross-correlation with respect to the cryo-EM density. The non-3D and 3D domain-swapped structures with low force field energy and best cross-correlation to the cryo-EM density were selected as best representative solutions. Further experimental details are described in Supplementary Note 1.

Europe PMC Funders Author Manuscripts

Extended Data

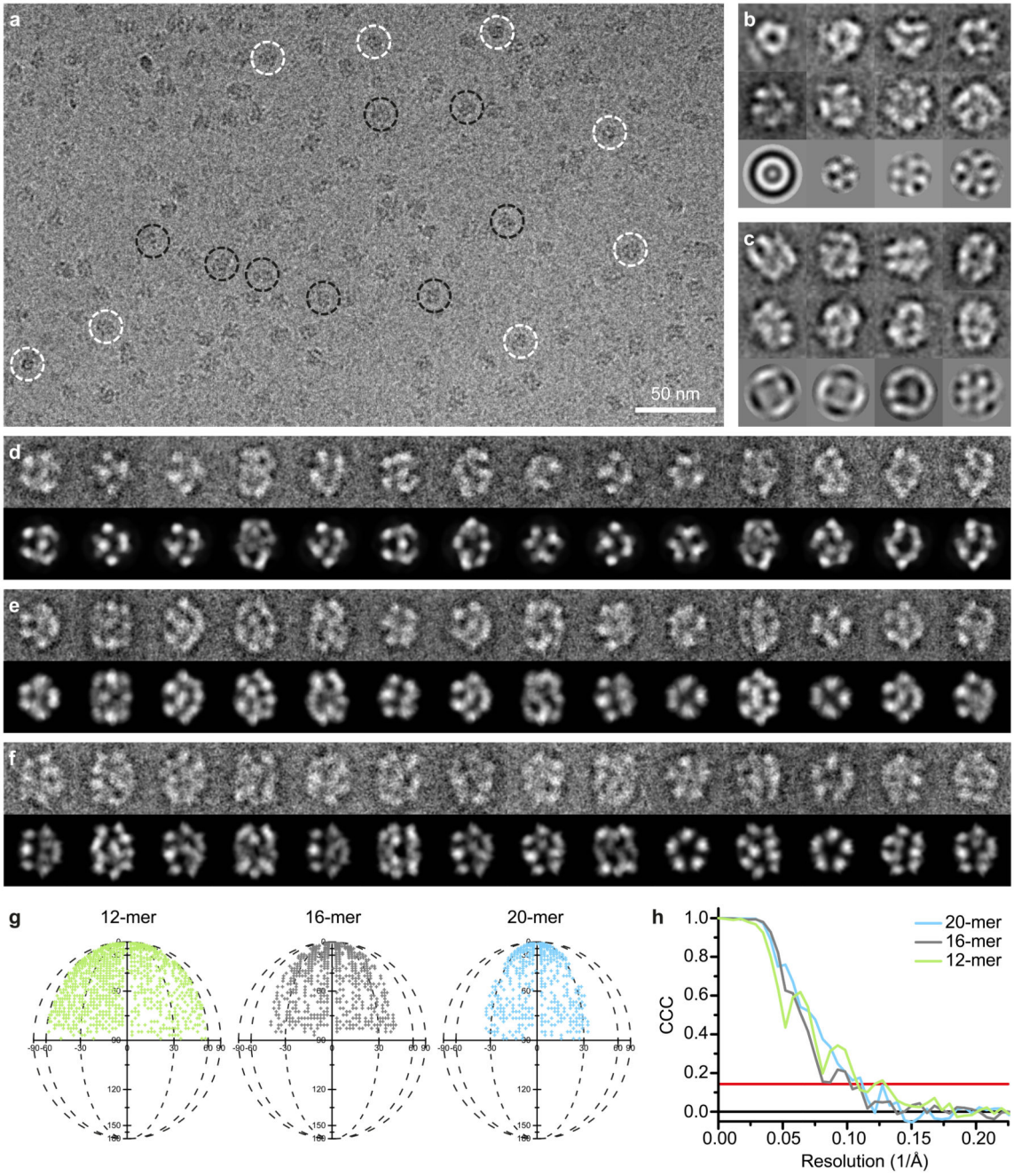

Extended Data Fig. 1. Cryo-EM/3D reconstruction of human αA-crystallin oligomers.
a) Cryo-EM micrograph of human αA-crystallin (reduced, αA_{red}). Top- and side-views are highlighted by white and black circles, respectively. Scale bar: 50 nm. **b**) Reference-free 2D class averages of top-views (top and middle rows) with corresponding eigenimages indicating size variations and 3-, 4- and 5-fold symmetries (bottom row). **c**) Reference-free 2D class averages of side-views (top and middle rows) with corresponding eigenimages

indicating 2-fold symmetry (bottom row). **d-f**) Characteristic final class averages (top row) with the corresponding 2D reprojections of the 3D model (bottom row) of the αA-crystallin 12-mer (**d**), 16-mer (**e**) and 20-mer (**f**). Box size in **b-f**, 17.3 nm. **g**) Angular distribution plots, i.e. the distributions of the Euler angles of the final class averages contributing to the 3D reconstructions of the αA-crystallin 12-, 16- and 20-mer. **h**) Fourier shell correlation (FSC) curves between maps from two independently refined half data sets of 12-, 16- and 20-mer populations. According to the 0.143 gold standard criterion, the resolutions for 12-, 16- and 20-mer 3D reconstructions are 9.2, 9.8 and 9.0 Å, respectively.

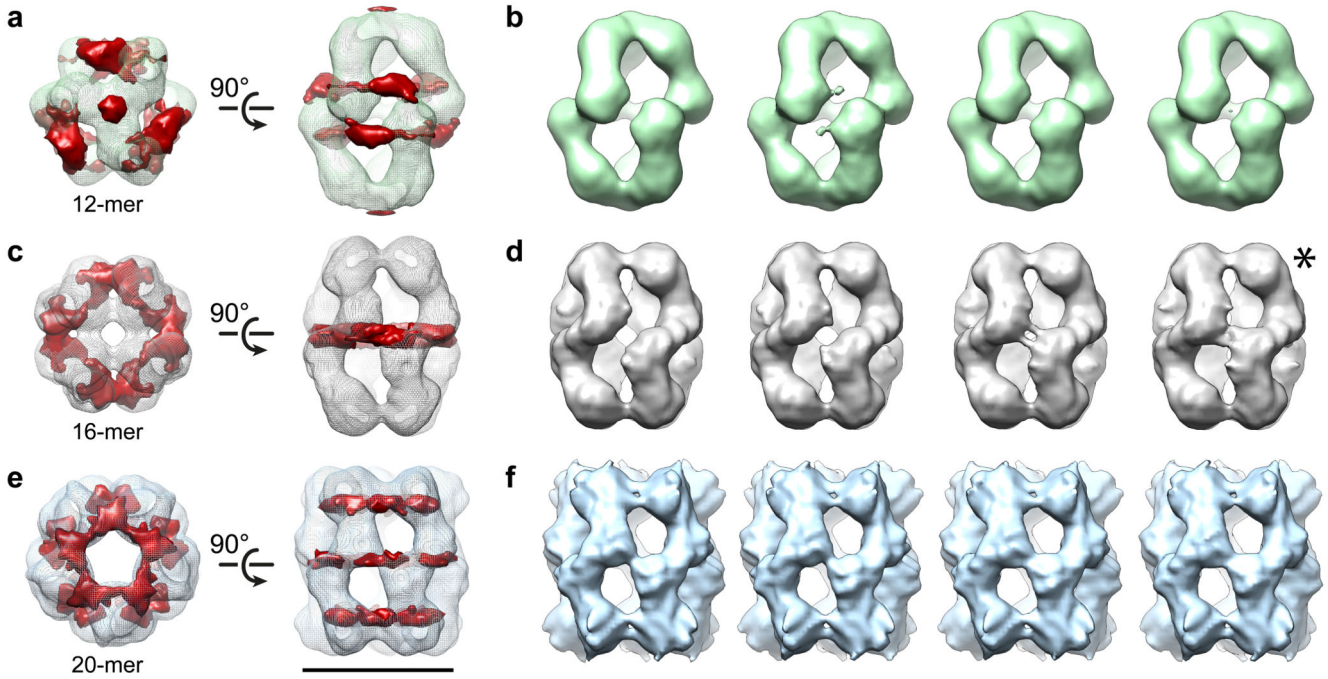

Extended Data Fig. 2. Structural variability of human αA-crystallin (reduced) oligomers.
a, c, e) Top and side views of the cryo-EM maps of αA-crystallin (reduced) 12-mer (**a**), 16-mer (**c**) and 20-mer (**e**) (mesh presentation) overlaid with the most important 3D eigenvector (red) indicating the positions of main variances (variance map). **b, d, f**) Representative 3D class averages of the 12-mer (**b**), 16-mer (**d**) and 20-mer (**f**). The map used for modeling of the 16-mer in 3D domain-swapped configuration is marked in (**d**) by an asterisk. Scale bar: 10 nm

Europe PMC Funders Author Manuscripts

Europe PMC Funders Author Manuscripts

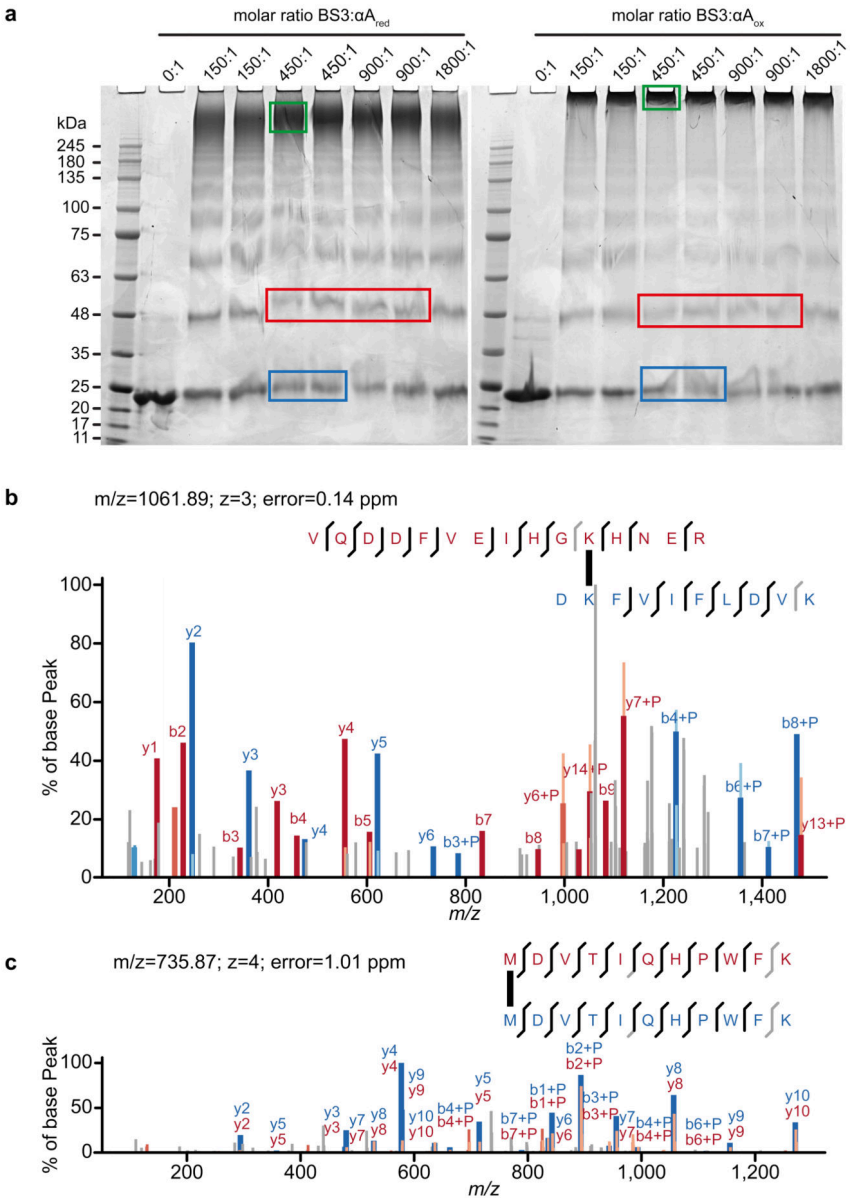

Extended Data Fig. 3. Cross-linking of human αA-crystallin.

a) Cross-linker titration of αA-crystallin, denaturing NuPAGE gel. Reduced (left) and oxidized (right) αA-crystallin were incubated for 1 h at room temperature with BS3 cross-linker at the indicated molar BS3:αA-crystallin ratios. Excised monomer (450:1, blue), dimer (450:1 and 900:1, red) and oligomer (450:1, green) gel bands for both αA_{red} and αA_{ox} were digested with trypsin and further analyzed. Sequence coverages: αA_{red}-monomer: 97.1 %, αA_{red}-dimer: 99.4 %, αA_{red}-oligomer: 100 %, αA_{ox}-monomer: 83.2 %, αA_{ox}-dimer: 94.8 %, αA_{ox}-oligomer: 100 %. **b**) Fragmentation spectrum of a cross-linked peptide with an intramolecular link between K70 and K99. **c**) Fragmentation spectrum of a cross-linked peptide with an intermolecular cross-link between M1 and M1.

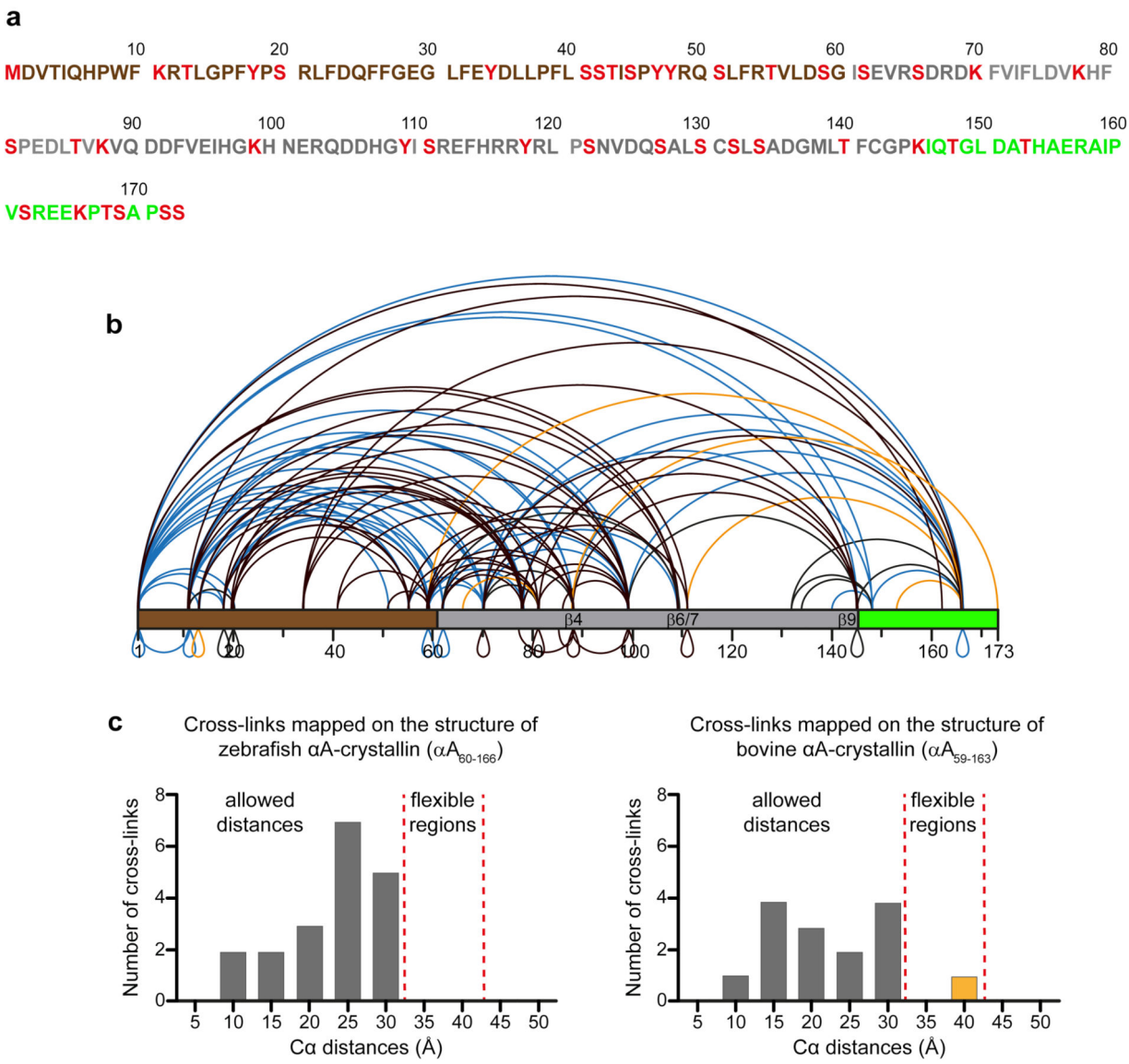

Extended Data Fig. 4. Cross-links observed in reduced and oxidized human αA-crystallin.

a) Primary sequence of human αA-crystallin. BS3 reactive K, S, T, Y residues and the N-terminus are coloured red. **b**) Linkage maps comparing the cross-linked residue pairs observed in monomer, dimer and oligomer pools of αA_{red} and αA_{ox}. In total, 113 auto-validation cross-links are shown. Colour code: blue, shared cross-links between αA_{red} and αA_{ox} (44 shared cross-links, 39 %); black, unique cross-links in αA_{ox} (63 cross-links, 56 %); orange, unique cross-links in αA_{red} (6 cross-links, 5 %). Colour code for the sequence regions of αA-crystallin: NTR (residues 1-60), sienna; ACD (residues 61-145), gray; CTR (residues 146-173), green. **c**) Histograms of Cα-Cα distances of cross-links observed in αA_{red}. The distances were measured between corresponding residues resolved in the crystal structures of truncated versions of zebrafish (PDB 3N3E, left) and bovine (PDB 3L1E, right) αA-crystallin.

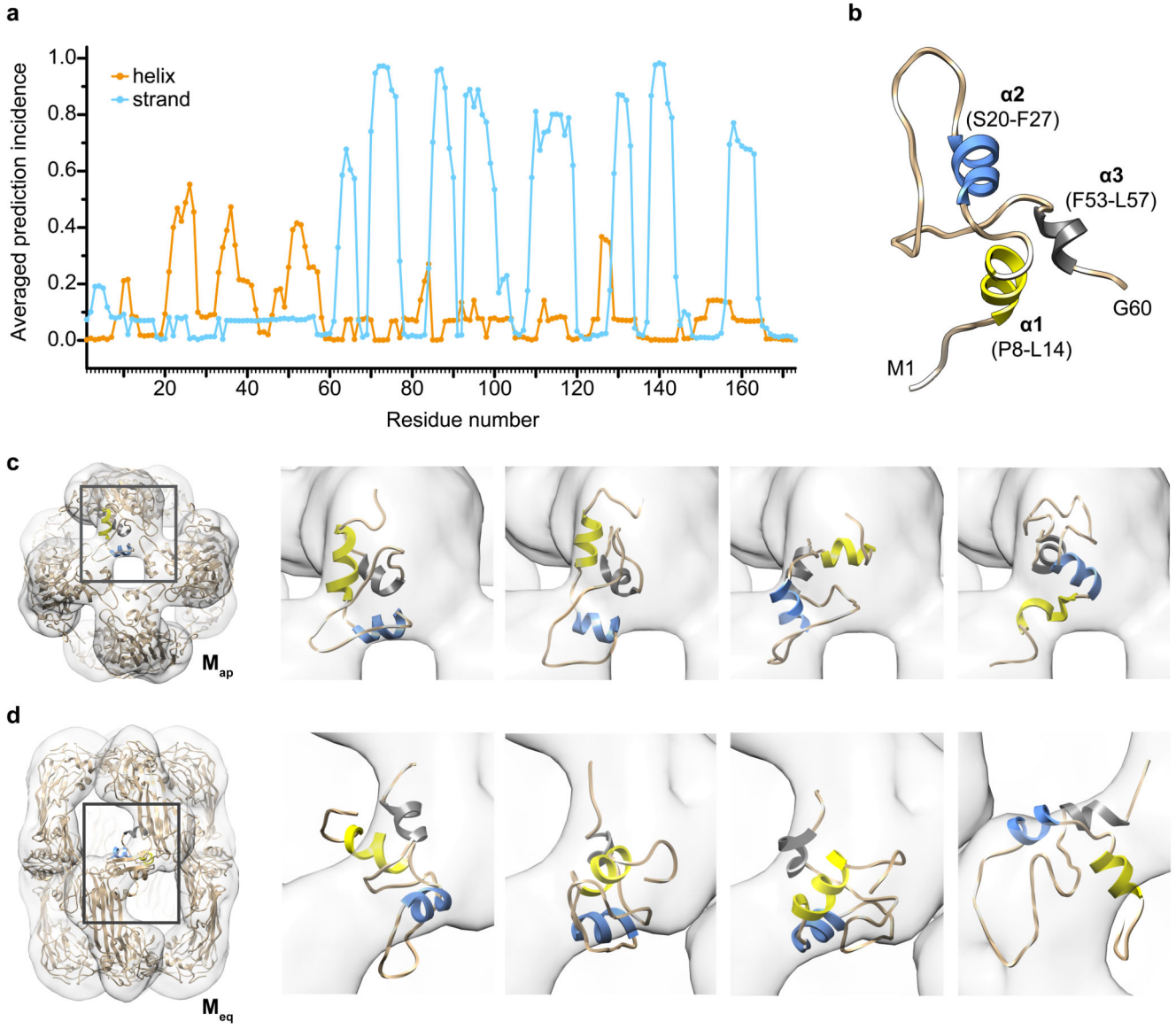

Extended Data Fig. 5. Secondary structure prediction and modeling of the N-terminal region of human αA-crystallin.

a) Summary of sequence-based secondary structure predictions of the NTR as obtained from 15 different web-based prediction programs. The predictions reproduce all β-strand segments (blue) present in metazoan sHsp structures. According to the predictions, the NTR most likely contains 3-4 α-helical segments (orange). **b**) A possible 3D structure model of the NTR of human αA-crystallin predicted using I-Tasser. **c**) Examples of possible conformations of the NTR of apical (M_{ap}) and **d**) equatorial protomers (M_{eq}) obtained upon structure modeling by molecular dynamics flexible fitting. Although the positions of the three helices within the EM-density in both M_{ap} and M_{eq} differ, their arrangement relative to each other is well preserved in comparison to the I-Tasser model (mRMSD ~2 Å).

Europe PMC Funders Author Manuscripts

Europe PMC Funders Author Manuscripts

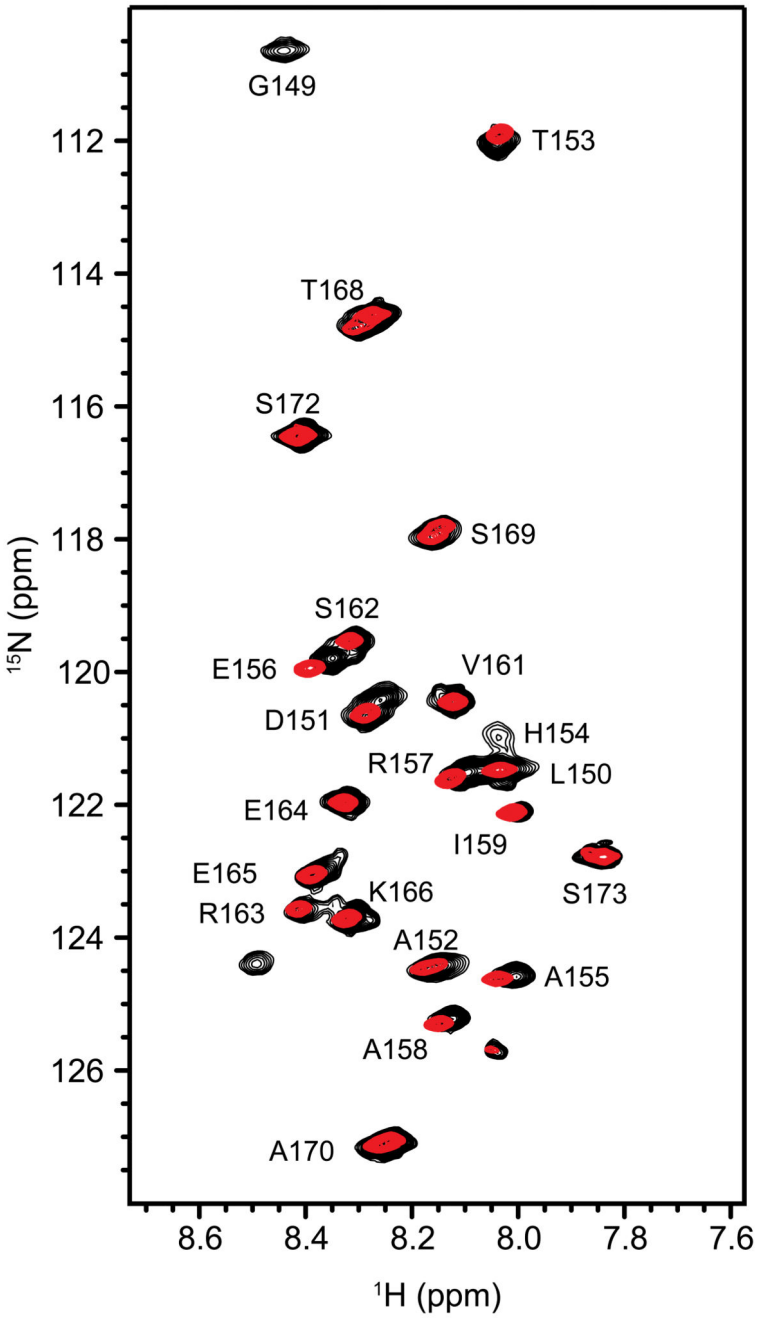

Extended Data Fig. 6. Superposition of $^{1}H,^{15}N$ correlation spectra of ^{15}N-αA$_{red}$ and ^{15}N-αA$_{red}$-IPSL.

The superposition of $^{1}H,^{15}N$ correlation spectra of ^{15}N-αA$_{red}$ (black) and ^{15}N-αA$_{red}$-IPSL treated with ascorbic acid (red) shows chemical shift perturbations for residues, for which we have observed an attenuation of the signal intensity for the oxidized ^{15}N-αA$_{red}$ -IPSL sample. In particular, residues T153, A155, E156, R157 display significant chemical shift changes, consistent with the PRE results. At the same time, the chemical shifts of the C-terminal residues (T168, S169, A170, S172, S173) are not affected by the presence of the nitroxyl moiety.

Europe PMC Funders Author Manuscripts

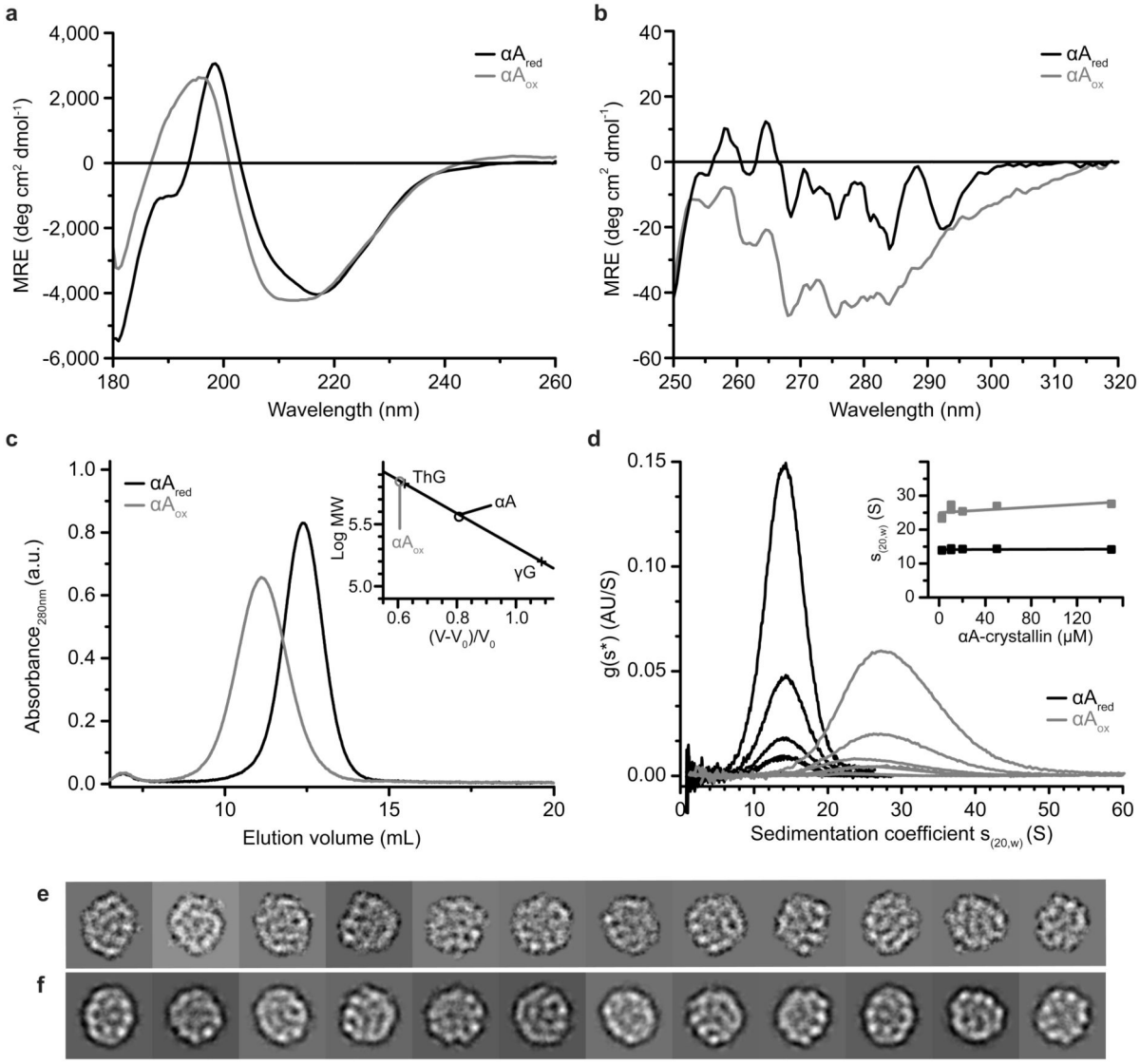

Extended Data Fig. 7. Impact of oxidation on αA-crystallin structure.

a) Far-UV and near-UV (**b**) CD spectra of αA_{red} (black line) and αA_{ox} (gray line). Note that the chemical microenvironment of tyrosins, phenylalanines and W9 are affected by oxidation. **c**) SEC elution profiles of αA_{red} (black line) and αA_{ox} (gray line) on a Superose 6 10/300 GL column. Inset: a segment of the calibration curve using the filtration standard mixture from BioRad. The calculated average molecular masses are 380 kDa for αA_{red} and 770 kDa for αA_{ox}, respectively (ThG: bovine thyroglobulin, 670 kDa; γG: bovine γ-globulin, 158 kDa). Note the peak broadening, that is increased polydispersity in αA_{ox}. **d**) Analysis of αA_{red} (black line) and αA_{ox} (gray line) by sedimentation velocity aUC in a concentration range from 2μM to 150 μM using SEDFIT. The concentrations are 2 μM, 10 μM, 20 μM, 50 μM and 150 μM. The inset shows the concentration dependence of the sedimentation coefficient. **e**) A set of the class averages used for the 3D reconstruction of αA_{ox} 32-mer. **f**) 2D reprojections of the reconstructed 3D volume corresponding to the orientations of the class averages shown in (**e**). Box size in (**e**) and (**f**): 26.7 nm.

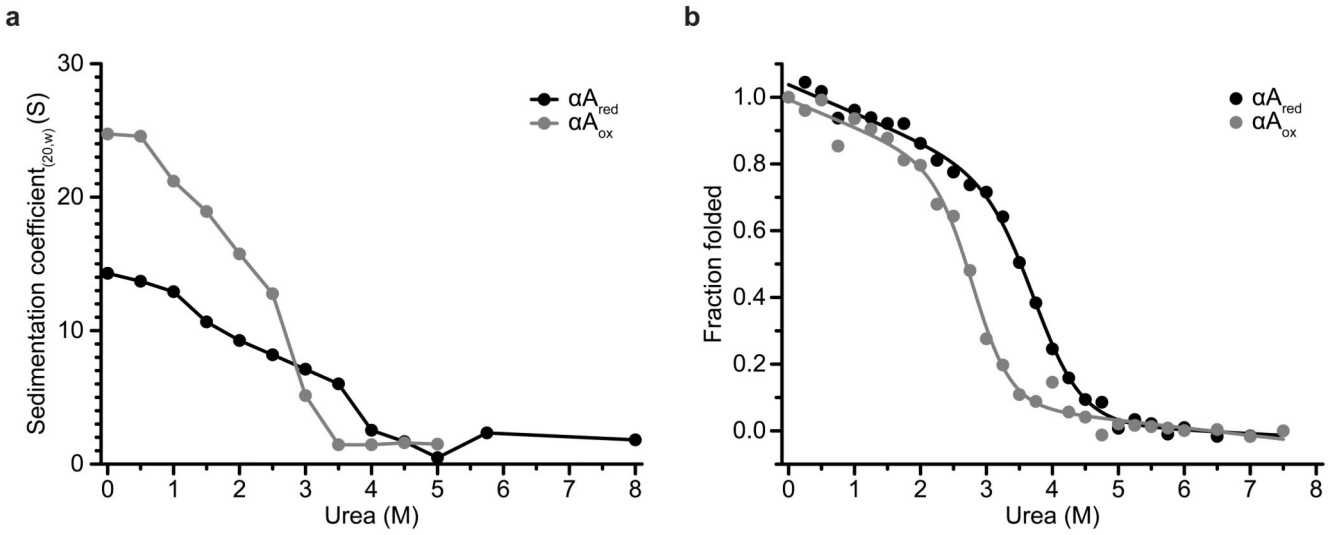

Extended Data Fig. 8. Impact of oxidation on αA-crystallin stability.

a) Oligomeric states of αA_{red} (black circles) and αA_{ox} (gray circles) in the presence of urea as determined by sedimentation velocity aUC at 20 °C. The oligomers of both proteins dissociate successively with increasing urea concentrations. Note that αA_{red} and αA_{ox} form a ~2 S species at urea concentrations of 4.5 M and 3.5 M, respectively, suggesting destabilization of αA_{ox} oligomers. **b**) Intrinsic fluorescence urea unfolding transitions for αA_{red} and αA_{ox} at 20 °C. The midpoints of the cooperative transition are at 2.7 M for αA_{ox} and at 3.8 M urea for αA_{red}, indicating destabilization of the NTR in the case of αA_{ox}. The spectral settings of the fluorimeter were chosen to selectively assess the transition of W9 located within the NTR.

Europe PMC Funders Author Manuscripts

Europe PMC Funders Author Manuscripts

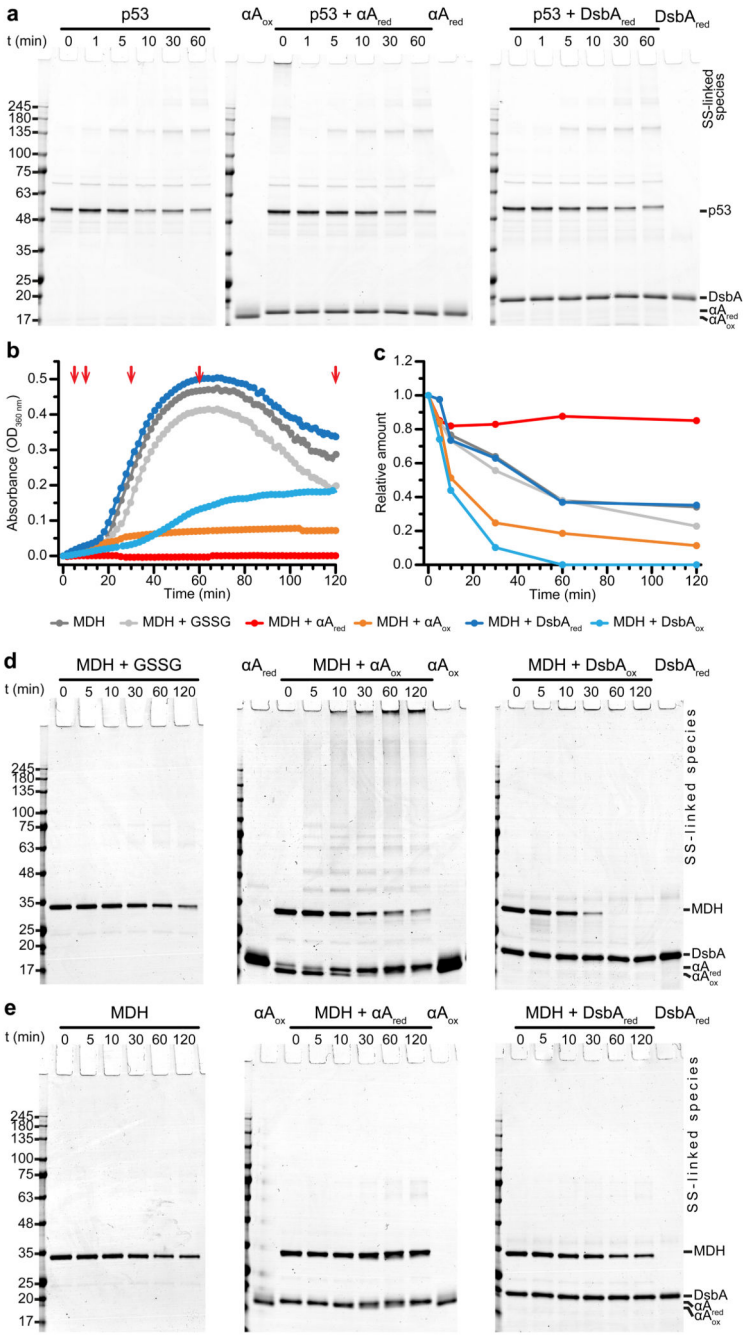

Extended Data Fig. 9. αA-crystallin is capable of transferring disulfide bonds to MDH.

a) Denaturing, non-reducing PAGE of samples withdrawn at the indicated timepoints (red arrows) from the aggregation assays in the presence of αA_{red} and recombinant reduced *E. coli* DsbA as shown in Fig. 7a. Note that disulfide-bridged species of p53 are formed only in marginal amounts. **b**) Heat-induced aggregation of recombinant malate dehydrogenase (MDH, 4μM) in the presence of an equimolar amount of GSSG, αA_{red}, αA_{ox} and reduced ($DsbA_{red}$) or oxidized ($DsbA_{ox}$) *E. coli* DsbA. Note that the aggregation of MDH is fully suppressed in the presence of αA_{red} and almost fully suppressed in the presence of αA_{ox}. **c**)

Relative intensity of the MDH monomer band as a fraction of the initial intensity (amount of monomer) at the beginning of each aggregation kinetics experiment (t = 0 min). **d,e**) Denaturing, non-reducing PAGE of samples withdrawn at the indicated timepoints (red arrows) from the aggregation assays shown in (**b**). Experiments were performed in the presence of GSSG, αA_{ox} or $DsbA_{ox}$ (**d**), in the absence of GSSG (MDH only) and in the presence of αA_{red} or $DsbA_{red}$ (**e**). Note that disulfide-bridged species of MDH are formed in the presence of αA_{ox}.

Supplementary Material

Refer to Web version on PubMed Central for supplementary material.

Acknowledgements

We are grateful to J. Plitzko (Max-Planck Institute for Biochemistry, Martinsried, Germany) for continuous support with electron microscopy and critical discussions. We thank D. Balchin for his comments on H/DX-MS data analysis, M.-L. Jokisch, R. Ciccone and G. Feind for technical assistance during initial experiments. This work was supported by grants from the Deutsche Forschungsgemeinschaft (SFB 1035) and CIPSM to J.B., B. Reif, M.Z. and S.W. Cross-linking/mass spectrometry work was supported by the Wellcome Trust (103139). The Wellcome Centre for Cell Biology is supported by core funding from the Wellcome Trust (203149).

Data Availability

The cryo-EM density maps of αA-crystallin oligomers have been deposited in the EMBD under accession codes EMD-4895 (12-mer), EMD-4894 (16-mer) and EMD-4896 (20-mer). The coordinates for the 16-mer model were deposited in the wwPDB under accession number PDB 6T1R. The mass spectrometry proteomics data have been deposited to the ProteomeXchange Consortium via the PRIDE partner repository with the dataset identifier PXD013587. The ^{1}H, ^{15}N, ^{13}C chemical shifts of reduced αA-crystallin are available at the BioMagResBank (BMRB) with the accession number BMRB-27109. All other data are available from the corresponding authors upon reasonable request.

References

1. Bloemendal H, et al. Ageing and vision: structure, stability and function of lens crystallins. Prog Biophys Mol Biol. 2004; 86:407–485. [PubMed: 15302206]
2. Clark AR, Lubsen NH, Slingsby C. sHSP in the eye lens: crystallin mutations, cataract and proteostasis. Int J Biochem Cell Biol. 2012; 44:1687–1697. [PubMed: 22405853]
3. Horwitz J. α-Crystallin can function as a molecular chaperone. Proc Natl Acad Sci USA. 1992; 89:10449–10453. [PubMed: 1438232]
4. Horwitz J. Alpha-crystallin. Exp Eye Res. 2003; 76:145–153. [PubMed: 12565801]
5. Graw J. Genetics of crystallins: cataract and beyond. Exp Eye Res. 2009; 88:173–189. [PubMed: 19007775]
6. Oguni M, et al. Ontogeny of alpha-crystallin subunits in the lens of human and rat embryos. Cell Tissue Res. 1994; 276:151–154. [PubMed: 8187157]
7. Iwaki T, Kume-Iwaki A, Liem RKH, Goldman JE. αB-crystallin is expressed in non-lenticular tissues and accumulates in Alexander's disease brain. Cell. 1989; 57:71–78. [PubMed: 2539261]
8. Srinivasan AN, Nagineni CN, Bhat SP. #x03B1;A-crystallin is expressed in non-ocular tissues. J Biol Chem. 1992; 267:23337–23341. [PubMed: 1429679]

9. Gangalum RK, Horwitz J, Kohan SA, Bhat SP. αA-crystallin and αB-crystallin reside in separate subcellular compartments in the developing ocular lens. J Biol Chem. 2012; 287:42407–42416. [PubMed: 23071119]
10. Datta SA, Rao CM. Differential temperature-dependent chaperone-like activity of αA- and αB-crystallin homoaggregates. J Biol Chem. 1999; 274:34773–34778. [PubMed: 10574947]
11. Reddy GB, Das KP, Petrash JM, Surewicz WK. Temperature-dependent chaperone activity and structural properties of human αA- and αB-crystallins. J Biol Chem. 2000; 275:4565–4570. [PubMed: 10671481]
12. Kumar LV, Ramakrishna T, Rao CM. Structural and functional consequences of the mutation of a conserved arginine residue in αA- and αB-crystallins. J Biol Chem. 1999; 274:24137–24141. [PubMed: 10446186]
13. Caspers GJ, Leunissen JA, de Jong WW. The expanding small heat-shock protein family, and structure predictions of the conserved 'α-crystallin domain'. J Mol Evol. 1995; 40:238–248. [PubMed: 7723051]
14. de Jong WW, Caspers GJ, Leunissen JA. Genealogy of the α-crystallin – small heat-shock protein superfamily. Int J Biol Macromol. 1998; 22:151–162. [PubMed: 9650070]
15. Laganowsky A, et al. Crystal structures of truncated alphaA and alphaB crystallins reveal structural mechanisms of polydispersity important for eye lens function. Protein Sci. 2010; 19:1031–1043. [PubMed: 20440841]
16. Laganowsky A, Eisenberg D. Non-3D domain swapped crystal structure of truncated zebrafish alphaA crystallin. Protein Sci. 2010; 19:1978–1984. [PubMed: 20669149]
17. Bova MP, Ding LL, Horwitz J, Fung BK. Subunit exchange of αA-crystallin. J Biol Chem. 1997; 272:29511–29517. [PubMed: 9368012]
18. Aquilina JA, et al. Subunit exchange of polydisperse proteins: mass spectrometry reveals consequences of αA-crystallin truncation. J Biol Chem. 2005; 280:14485–1449. [PubMed: 15701626]
19. Peschek J, et al. The eye lens chaperone α-crystallin forms defined globular assemblies. Proc Natl Acad Sci USA. 2009; 106:13272–13277. [PubMed: 19651604]
20. Merck KB, de Haard-Hoekman WA, Essink BBO, Bloemendal H, de Jong WW. Expression and aggregation of recombinant αA-crystallin and its two domains. Biochim Biophys Acta. 1992; 1130:267–276. [PubMed: 1562604]
21. Bova MP, Mchaourab HS, Han Y, Fung BKK. Subunit exchange of small heat shock proteins. Analysis of oligomer formation of αA-crystallin and Hsp27 by fluorescence resonance energy transfer and site-directed truncations. J Biol Chem. 2000; 275:1035–1042. [PubMed: 10625643]
22. Salerno JC, Eifert CL, Salerno KM, Koretz JF. Structural diversity in the small heat shock protein superfamily: control of aggregation by the N-terminal region. Protein Eng. 2003; 16:847–851. [PubMed: 14631074]
23. Kundu M, Sen PC, Das KP. Structure, stability, and chaperone function of αA-crystallin: role of N-terminal region. Biopolymers. 2007; 86:177–192. [PubMed: 17345631]
24. Andley UP, Mathur S, Griest TA, Petrash JM. Cloning, expression, and chaperone-like activity of human αA-crystallin. J Biol Chem. 1996; 271:31973–31980. [PubMed: 8943244]
25. Thampi P, Abraham EC. Influence of the C-terminal residues on oligomerization of αA-crystallin. Biochemistry. 2003; 42:11857–11863. [PubMed: 14529298]
26. Rajan S, Chandrashekar R, Aziz A, Abraham EC. Role of arginine-163 and the ^{163}REEK^{166} motif in the oligomerization of truncated α-crystallins. Biochemistry. 2006; 45:15684–15691. [PubMed: 17176090]
27. Aziz A, Santhoshkumar P, Sharma KK, Abraham EC. Cleavage of the C-terminal serine of human αA-crystallin produces αA_{1-172} with increased chaperone activity and oligomeric size. Biochemistry. 2007; 46:2510–2519. [PubMed: 17279772]
28. Treweek TM, Rekas A, Walker MJ, Carver JA. A quantitative NMR spectroscopic examination of the flexibility of the C-terminal extensions of the molecular chaperones, αA- and αB-crystallin. Exp Eye Res. 2010; 91:691–699. [PubMed: 20732317]
29. Kim KK, Kim R, Kim SH. Crystal structure of a small heat-shock protein. Nature. 1998; 394:595–599. [PubMed: 9707123]

30. van Montfort RL, Basha E, Friedrich KL, Slingsby C, Vierling E. Crystal structure and assembly of a eukaryotic small heat shock protein. Nat Struct Biol. 2001; 8:1025–1030. [PubMed: 11702068]
31. Runkle S, Hill J, Kantorow M, Horwitz J, Posner M. Sequence and spatial expression of zebrafish (*Danio rerio*) αA-crystallin. Mol Vis. 2002; 8:45–50. [PubMed: 11925526]
32. Augusteyn RC, Hum TP, Putilin TP, Thomson JA. The location of sulphydryl groups in α-crystallin. Biochim Biophys Acta. 1987; 915:132–139. [PubMed: 3620480]
33. Srikanthan D, Bateman OA, Purkiss AG, Slingsby C. Sulfur in human crystallins. Exp Eye Res. 2004; 79:823–831. [PubMed: 15642319]
34. Miesbauer LR, et al. Post-translational modifications of water-soluble human lens crystallins from young adult. J Biol Chem. 1994; 269:12494–12502. [PubMed: 8175657]
35. Takemoto LJ. Oxidation of cysteine residues from alpha-A crystallin during cataractogenesis of the human lens. Biochem Biophys Res Commun. 1996; 223:216–220. [PubMed: 8670261]
36. Takemoto LJ. Increase in the intramolecular disulfide bonding of alpha-A crystallin during aging of the human lens. Exp Eye Res. 1996; 63:585–590. [PubMed: 8994362]
37. Hains PG, Truscott RJW. Proteomic analysis of the oxidation of cysteine residues in human age-related nuclear cataract lenses. Biochim Biophys Acta. 2008; 1784:1959–1964. [PubMed: 18761110]
38. Fan X, et al. Evidence of highly conserved β-crystallin disulfidome that can be mimicked by *in vitro* oxidation in age-related human cataract and glutathione depleted mouse lens. Mol Cell Proteomics. 2015; 14:3211–3223. [PubMed: 26453637]
39. Yang Z, Chamorro M, Smith DL, Smith JB. Identification of the major components of the high molecular weight crystallins from old human lenses. Curr Eye Res. 1994; 13:415–421. [PubMed: 7924405]
40. Lund AL, Smith JB, Smith DL. Modifications of the water-insoluble human lens α-crystallins. Exp Eye Res. 1996; 63:661–672. [PubMed: 9068373]
41. Hanson SRA, Hasan A, Smith DL, Smith JB. The major in vivo modifications of the human water-insoluble lens crystallins are disulfide bonds, deamidation, methionine oxidation, and backbone cleavage. Exp Eye Res. 2000; 71:195–207. [PubMed: 10930324]
42. Cherian-Shaw M, Smith JB, Jiang XY, Abraham EC. Intrapolypeptide disulfides in human αA-crystallin and their effect on chaperone-like function. Mol Cell Biochem. 1999; 199:163–167. [PubMed: 10544964]
43. Merkley ED, et al. Distance restraints from crosslinking mass spectrometry: Mining a molecular dynamics simulation database to evaluate lysine–lysine distances. Protein Sci. 2014; 23:747–759. [PubMed: 24639379]
44. Dyson HJ, Wright PE. Unfolded proteins and protein folding studied by NMR. Chem Rev. 2004; 104:3607–3622. [PubMed: 15303830]
45. Clore GM, Iwahara J. Theory, Practice, and Applications of Paramagnetic Relaxation Enhancement for the Characterization of Transient Low-Population States of Biological Macromolecules and Their Complexes. Chem Rev. 2009; 109:4108–4139. [PubMed: 19522502]
46. Chakraborty K, et al. Protein stabilization by introduction of cross-strand disulfides. Biochemistry. 2005; 44:14638–14646. [PubMed: 16262263]
47. Wunderlich M, Glockshuber R. Redox properties of protein disulfide isomerase (DsbA) from *Escherichia coli* . Protein Sci. 1993; 2:717–726. [PubMed: 8495194]
48. Zapun A, Missiakas D, Raina S, Creighton TE. Structural and functional characterization of DsbC, a protein involved in disulfide bond formation in *Escherichia coli* . Biochemistry. 1995; 34:5075–89. [PubMed: 7536035]
49. Hasan A, Yu J, Smith DL, Smith JB. Thermal stability of human α-crystallins sensed by amide hydrogen exchange. Protein Sci. 2004; 13:332–341. [PubMed: 14739319]
50. Jehle S, et al. N-terminal domain of αB-crystallin provides a conformational switch for multimerization and structural heterogeneity. Proc Natl Acad Sci USA. 2011; 108:6409–6414. [PubMed: 21464278]
51. Mainz A, et al. The chaperone αB-crystallin uses different interfaces to capture an amorphous and an amyloid client. Nat Struct Mol Biol. 2015; 22:898–905. [PubMed: 26458046]

52. Sluchanko NN, et al. Structural basis for the interaction of a human small heat shock protein with the 14–3–3 universal signaling regulator. Structure. 2017; 25:305–316. [PubMed: 28089448]
53. Pasta Y, Raman B, Ramakrishna T, Rao CM. Role of the conserved SRLFDQFFG region of α-crystallin, a small heat shock protein. Effect on oligomeric size, subunit exchange, and chaperone-like activity. J Biol Chem. 2003; 278:51159–51166. [PubMed: 14532291]
54. Baldwin A, et al. Quaternary dynamics of αB-crystallin as a direct consequence of localised tertiary fluctuations in the C-terminus. J Mol Biol. 2011; 413:310–320. [PubMed: 21839749]
55. Alderson TR, Benesch JLP, Baldwin AJ. Proline isomerization in the C-terminal region of HSP27. Cell Stress Chaperones. 2017; 22:639–651. [PubMed: 28547731]
56. Jehle S, et al. Solid-state NMR and SAXS studies provide a structural basis for the activation of αB-crystallin oligomers. Nat Struct Mol Biol. 2010; 17:1037–1042. [PubMed: 20802487]
57. Braun N, et al. Multiple molecular architectures of the eye lens chaperone αB-crystallin elucidated by a triple hybrid approach. Proc Natl Acad Sci USA. 2011; 108:20491–20496. [PubMed: 22143763]
58. Pasta SY, Raman B, Ramakrishna T, Rao CM. The IXI/V motif in the C-terminal extension of α-crystallins: alternative interactions and oligomeric assemblies. Mol Vis. 2004; 10:655–662. [PubMed: 15448619]
59. Li Y, Schmitz KR, Salerno JC, Koretz JF. The role of the conserved COOH-terminal triad in αA-crystallin aggregation and functionality. Mol Vis. 2007; 13:1758–1768. [PubMed: 17960114]
60. Alderson TR, et al. Local unfolding of the HSP27 monomer regulates chaperone activity. Nat Commun. 2019; 10
61. Chen J, Feige M, Franzmann TM, Bepperling A, Buchner J. Regions outside the α-crystallin domain of the small heat shock protein Hsp26 are required for its dimerization. J Mol Biol. 2010; 398:122–131. [PubMed: 20171228]
62. Huber-Wunderlich M, Glockshuber R. A single dipeptide sequence modulates the redox properties of a whole enzyme family. Fold Des. 1998; 3:161–171. [PubMed: 9562546]
63. Bova LM, Sweeney MH, Jamie JF, Truscott RJW. Major changes in human ocular UV protection with age. Invest Ophthalmol Vis Sci. 2001; 42:200–205. [PubMed: 11133868]
64. Grey AC, Demarais NJ, Brandi J, West BJ, Donaldson PJ. A quantitative map of glutathione in the aging human lens. Int J Mass Spectrom. 2017; 437:58–68.
65. Hogg PJ. Disulfide bonds as switches for protein function. Trends Biochem Sci. 2003; 28:210–214. [PubMed: 12713905]
66. Lou MF. Redox regulation in the lens. Prog Retin Eye Res. 2003; 22:657–682. [PubMed: 12892645]
67. Rost J, Rapoport S. Reduction-potential of glutathione. Nature. 1964; 201:185.
68. Simpson RJ. Estimation of free thiols and disulfide bonds using Ellman's reagent. Cold Spring Harb Protoc. 2008; 9:1–8.
69. Stafford WF. Boundary analysis in sedimentation transport experiments: a procedure for obtaining sedimentation coefficient distributions using the time derivative of the concentration profile. Anal Biochem. 1992; 203:295–301. [PubMed: 1416025]
70. Royer CA, Mann CJ, Matthews CR. Resolution of the fluorescence equilibrium unfolding profile of trp aporepressor using single tryptophan mutants. Protein Sci. 1993; 11:1844–1852.
71. Wei H, et al. Using hydrogen/deuterium exchange mass spectrometry to study conformational changes in granulocyte colony stimulating factor upon PEGylation. J Am Soc Mass Spectrom. 2012; 23:498–504. [PubMed: 22227798]
72. Korinek A, Beck F, Baumeister W, Nickell S, Plitzko JM. Computer controlled cryo-electron microscopy - TOM^2 a software package for high-throughput applications. J Struct Biol. 2011; 175:394–405. [PubMed: 21704708]
73. Tang G, et al. EMAN2: an extensible image processing suite for electron microscopy. J Struct Biol. 2007; 157:38–46. [PubMed: 16859925]
74. Heymann JB, Belnap DM. Bsoft: Image processing and molecular modeling for electron microscopy. J Struct Biol. 2007; 157:3–18. [PubMed: 17011211]

75. van Heel M, Harauz G, Orlova EV, Schmidt R, Schatz M. A new generation of the IMAGIC image processing system. J Struct Biol. 1996; 116:17–24. [PubMed: 8742718]
76. van Heel M. Angular reconstitution: a posteriori assignment of projection directions for 3D reconstruction. Ultramicroscopy. 1987; 21:111–123. [PubMed: 12425301]
77. Rosenthal PB, Henderson R. Optimal determination of particle orientation, absolute hand, and contrast loss in single-particle electron cryomicroscopy. J Mol Biol. 2003; 333:721–745. [PubMed: 14568533]
78. Lawson CL, et al. EMDataBank unified data resource for 3DEM. Nucleic Acids Res. 2016; 44:D386–D403.
79. Goddard TD, Huang CC, Ferrin TE. Visualizing density maps with UCSF Chimera. J Struct Biol. 2007; 157:281–287. [PubMed: 16963278]
80. Penczek PA, Yang C, Frank J, Spahn CM. Estimation of variance in single-particle reconstruction using the bootstrap technique. J Struct Biol. 2006; 154:168–183. [PubMed: 16510296]
81. Maiolica A, et al. Structural analysis of multiprotein complexes by cross-linking, mass spectrometry, and database searching. Mol Cell Proteomics. 2007; 6:2200–2211. [PubMed: 17921176]
82. Cox J, Mann M. MaxQuant enables high peptide identification rates, individualized p.p.b.-range mass accuracies and proteome-wide protein quantification. Nat Biotechnol. 2008; 26:1367–1372. [PubMed: 19029910]
83. Mendes ML, et al. An integrated workflow for crosslinking mass spectrometry. Mol Syst Biol. 2019; 15:e8994. [PubMed: 31556486]
84. Fischer L, Rappsilber J. Quirks of error estimation in cross-linking/mass spectrometry. Anal Chem. 2017; 89:3829–3833. [PubMed: 28267312]
85. Webb B, Sali A. Comparative protein structure modeling using MODELLER. Curr Protoc Bioinformatics. 2014; 47:1–32. [PubMed: 25199789]
86. Roy A, Kucukural A, Zhang Y. I-TASSER: A unified platform for automated protein structure and function prediction. Nat Protoc. 2010; 5:725–738. [PubMed: 20360767]
87. Chacón P, Wriggers W. Multi-resolution contour-based fitting of macromolecular structures. J Mol Biol. 2002; 317:375–384. [PubMed: 11922671]
88. Case, DA, , et al. AMBER 16. University of California; San Francisco: 2016.
89. Wu X, Subramaniam S, Case DA, Wu KW, Brooks BR. Targeted conformational search with map-restrained self-guided Langevin dynamics: application to flexible fitting into electron microscopic density maps. J Struct Biol. 2013; 183:429–440. [PubMed: 23876978]

Reporting Summary

Further information on experimental design is available in the Nature Research Reporting Summary linked to this article.

Europe PMC Funders Author Manuscripts

Europe PMC Funders Author Manuscripts

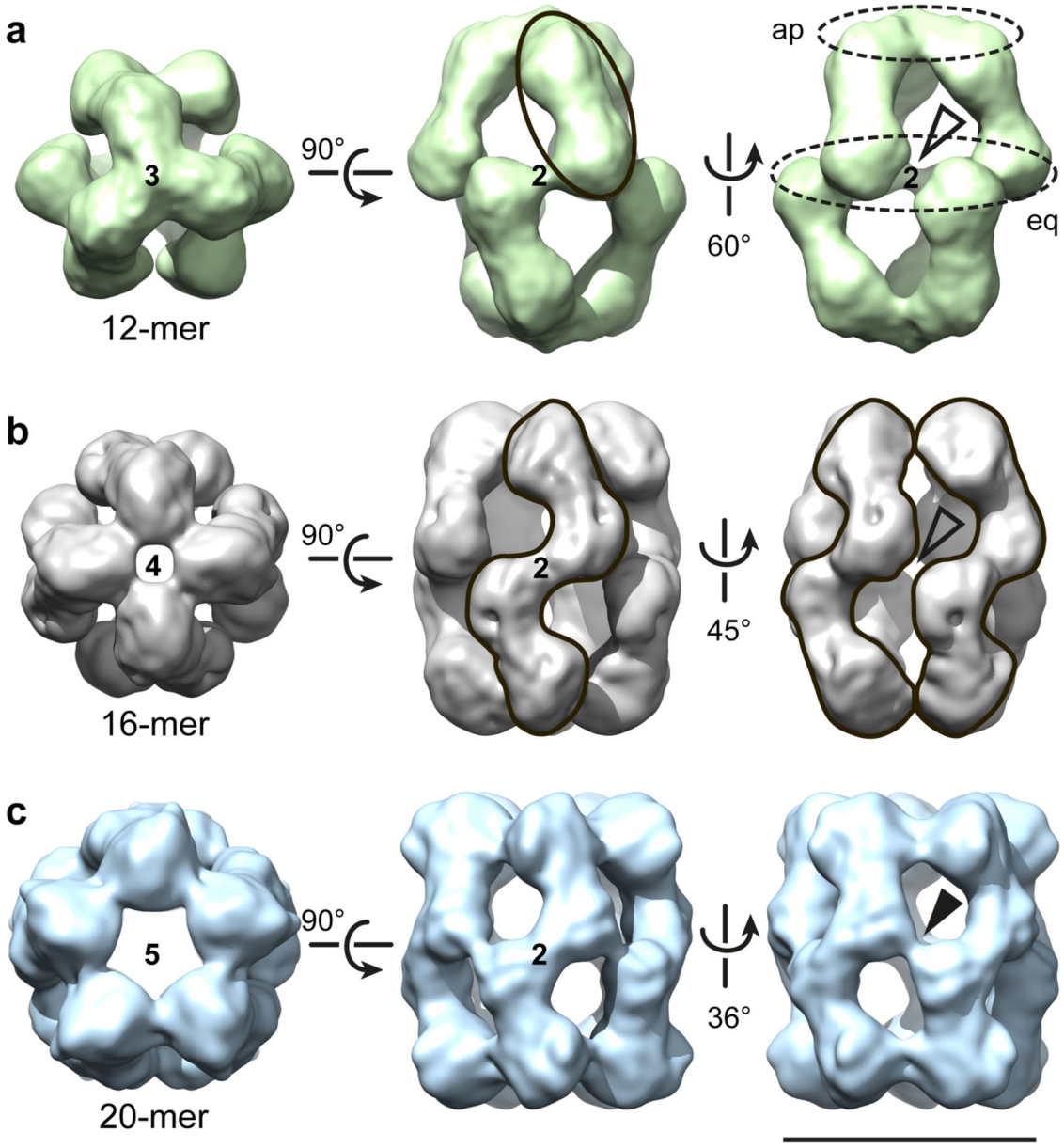

Figure 1. Cryo-EM 3D-reconstructions of human αA-crystallin (reduced) oligomers.

a) 12-mer (D3 symmetry) viewed along a 3-fold (left, top view) and 2-fold symmetry axis (middle, right; side views). The volume corresponding to an αA-crystallin dimer is indicated by a black ellipse (middle). Apical (ap) and equatorial (eq) regions of the barrel-shaped 12-mer are marked by dashed ellipses. **b, c)** Top and side views of the 16-mer (D4 symmetry) (**b**) and of the 20-mer (D5 symmetry) (**c**). For clarity, three tetramers of the 16-mer are outlined. The open arrowheads in (**a**) and (**b**) indicate the missing density between two adjacent tetramers in the equatorial plane of the barrel, and the filled arrowhead in (**c**) indicates the inter-tetramer density. Scale bar: 10 nm. The isosurface thresholds were set to render a volume corresponding to a protein mass of 239 kDa for the 12-mer, 319 kDa for the 16-mer, and 398 kDa for the 20-mer.

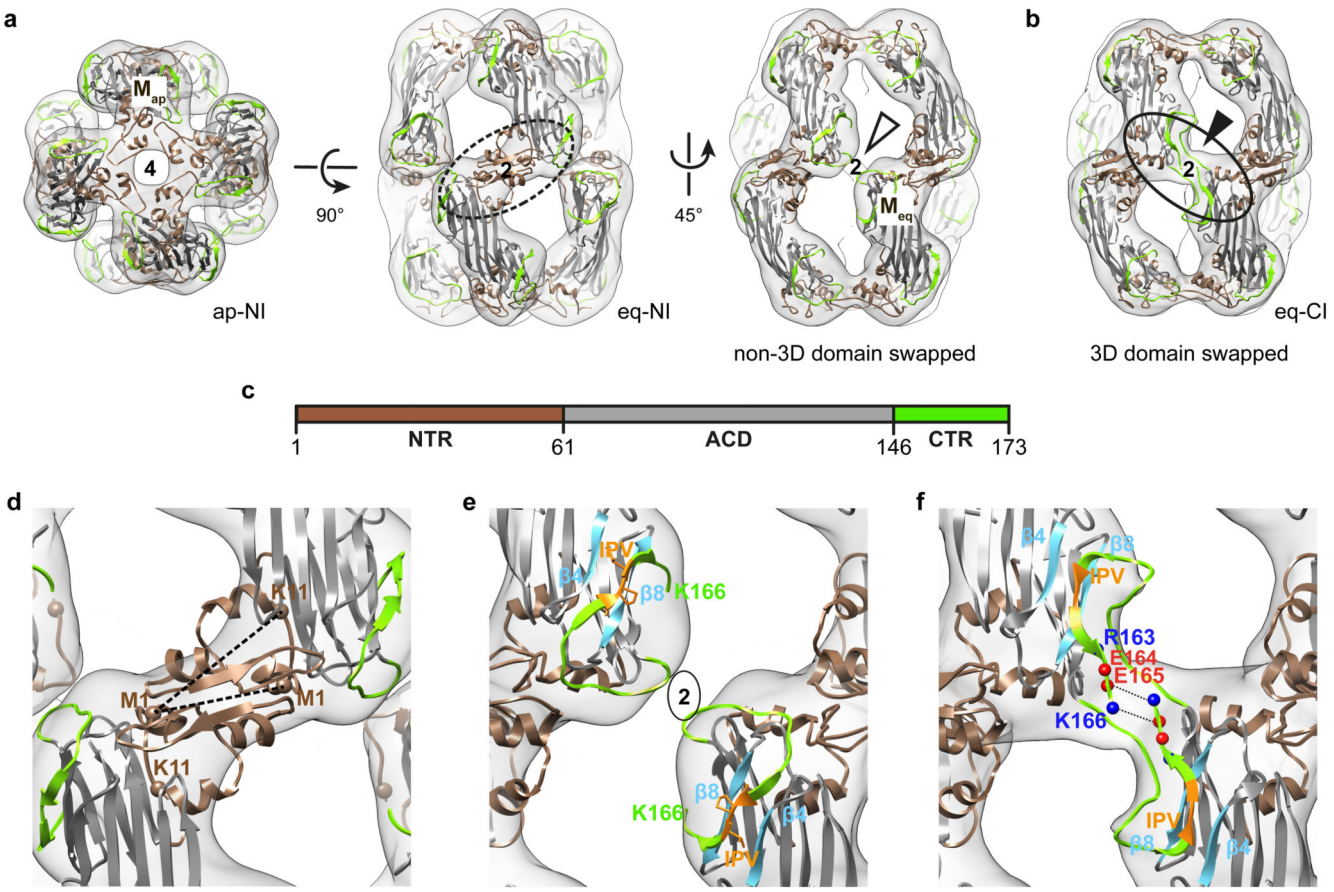

Figure 2. Pseudoatomic models of the human αA-crystallin (reduced) 16-mer.

a) Top and side views of the cryo-EM map of the αA-crystallin 16-mer (reduced) superimposed with the atomic model (ribbon representation) containing the CTRs of apical (M_{ap}) and equatorial (M_{eq}) protomers in a non-3D domain-swapped conformation. ap-NI: apical N-terminal interface; eq-NI: equatorial N-terminal interface (black dashed ellipse). **b**) 16-mer containing the CTRs of M_{eq} in a 3D domain-swapped conformation. eq-CI: equatorial C-terminal interface (black solid ellipse). **c**) The domain organization of human αA-crystallin (NTR, residues 1–60, sienna; ACD, residues 61–145, gray; CTR, residues 146-173, green). **d**) Close-up view of the eq-NI with intermolecular cross-links involving the residues M1 and K11. **e**) Close-up view of two neighboring equatorial protomers (eq-CI) with their CTRs in the non-3D domain-swapped configuration shown in (**a**). The IPV motifs are shown in orange, β4- and β8-strands in light blue. **f**) Close-up view of eq-CI of the 3D domain-swapped model shown in (**b**). Negatively and positively charged residues located within the CTRs are shown in red and blue, respectively.

Europe PMC Funders Author Manuscripts

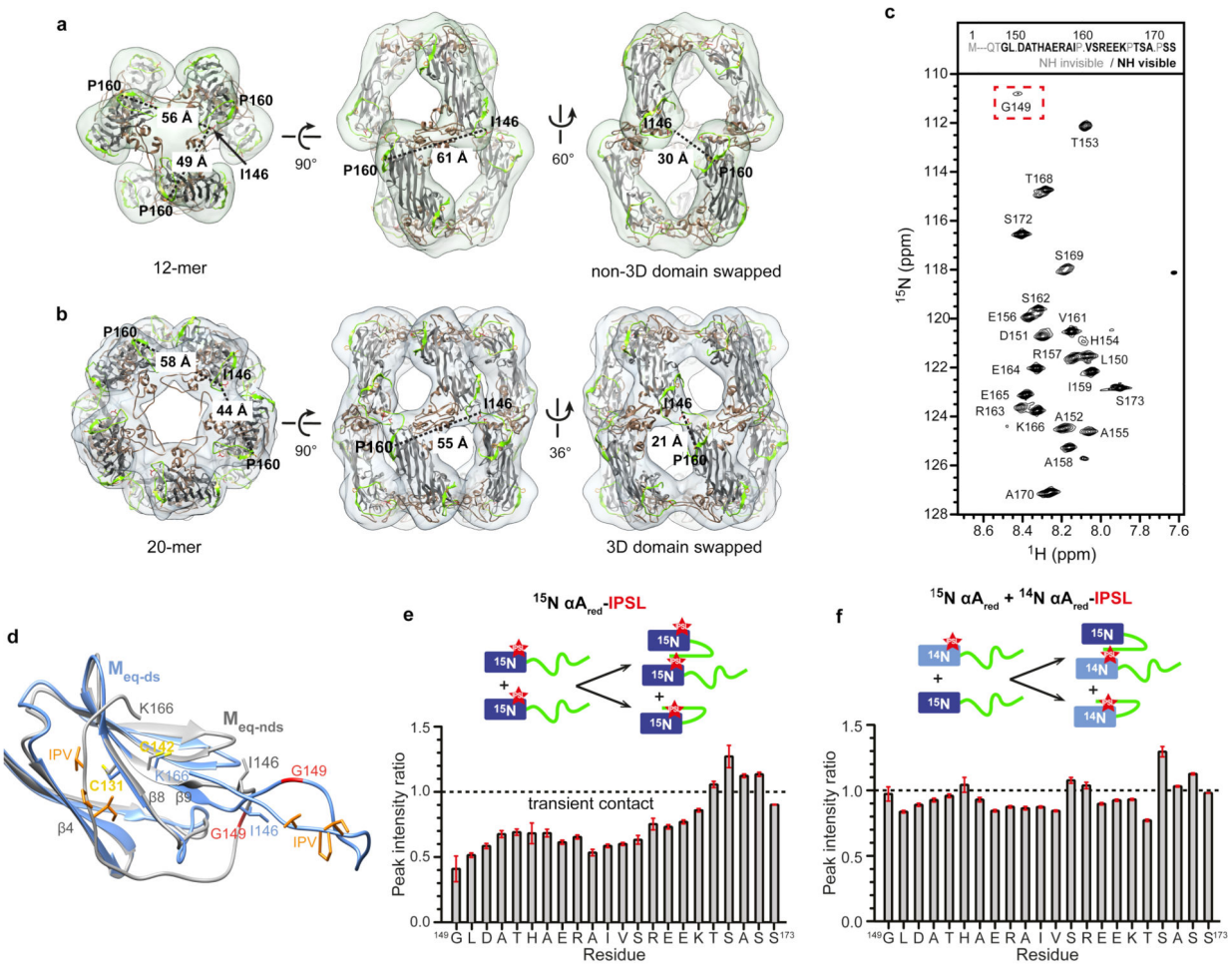

Figure 3. CTR interactions in the reduced αA-crystallin oligomer ensemble.

a) The αA_{red} 12-mer superimposed with the pseudoatomic model containing the CTRs of both M_{ap} and M_{eq} in a non-3D domain-swapped conformation. **b**) The αA_{red} 20-mer superimposed with the pseudoatomic model containing the CTRs of M_{eq} in a 3D domain-swapped conformation. Domain color coding is as in Fig. 2. Dashed lines indicate the inter-protomer distances (measured as the distance between I146 and P160 of neighboring protomers) to be spanned by the linker between β9 and β10 for 3D domain-swap. **c**) ^{1}H, ^{15}N HSQC solution-state NMR spectrum of αA_{red}. In the inset, assigned backbone resonances involving the residues G149-S173 are shown in black, and non-detectable residues in gray. **d**) Alignment of an equatorial, non-3D domain-swapped protomer ($M_{eq\text{-}nds}$, gray) with an equatorial, 3D domain-swapped protomer ($M_{eq\text{-}ds}$, blue). The positions of C131, C142, G149 and of the IPV motif are indicated. **e**) PRE intensity ratios of a ^{15}N- and spin-labeled sample (^{15}N-αA_{red}-IPSL) as a function of the residue number. As the spin label is attached to ^{15}N-labeled protein, intra- and intermolecular PREs are not distinguishable. **f**) PRE intensity ratios of a mixed sample containing ^{15}N-labeled αA_{red} (^{15}N-αA_{red}) and unlabeled protein bearing the spin label (^{14}N-αA_{red}-IPSL) in a 1:1 ratio (^{15}N-αA_{red}+^{14}N-αA_{red}-IPSL). As the spin label is attached to ^{14}N-αA, only intermolecular contacts lead to signal

quenching. For (**e**) and (**f**), the experimental error was determined from the signal-to-noise ratios of the individual cross peaks (details are outlined in Supplementary Note 1).

Europe PMC Funders Author Manuscripts

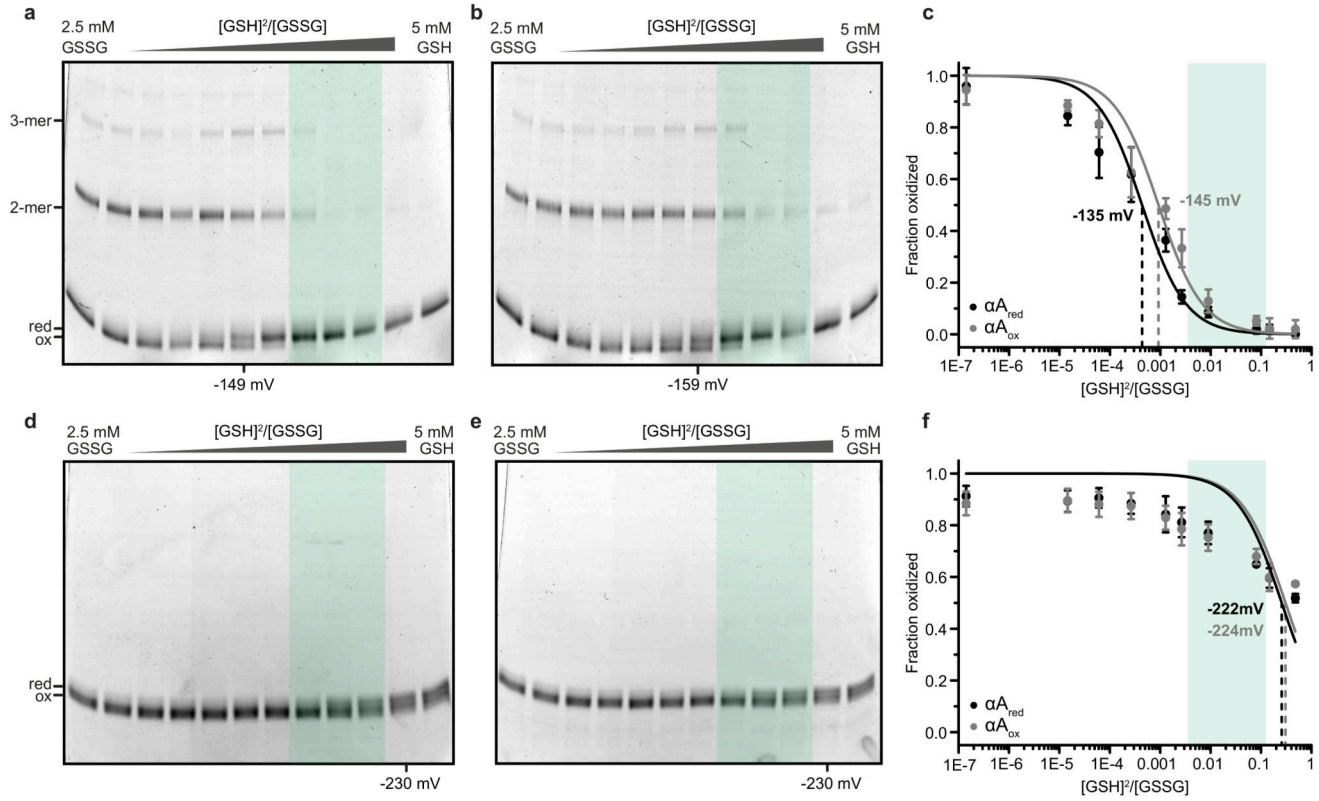

Figure 4. Intramolecular disulfide cross-linking in human αA-crystallin.

a) Denaturing, non-reducing polyacrylamide gel electrophoresis (PAGE) of αA_{red} incubated at 43 °C for 20 h in the presence of different GSH:GSSG ratios from fully oxidizing (2.5 mM GSSG) to fully reducing (5 mM GSH) conditions. GSSG: oxidized glutathione; GSH: reduced glutathione; ox: oxidized monomeric αA-crystallin; red: reduced monomeric αA-crystallin; 2-mer and 3-mer, disulfide-linked dimers and trimers. Note that even in the presence of 5 mM GSH, minute amounts of intermolecular disulfide-bonded dimers form, likely as a result of GSSG impurities present in the commercial GSH preparation. **b**) The same titration as in (**a**) but using αA_{ox} at the reaction start. **c**) Relative intensities of the αA_{red} and αA_{ox} monomer bands of gels as shown in (**a**) and (**b**) as a function of the $[GSH]^2$:[GSSG] ratio. Half-maximal oxidation (dashed line) at a redox potential of -135 mV (black, K_{eq}: 0.434 mM) for αA_{red} and at -145 mV (gray, K_{eq}: 0.92 mM) for αA_{ox}. **d**) Denaturing, non-reducing PAGE of αA_{red} incubated for 20 h at 43 °C in the presence of 4.5 M urea and at varying GSH:GSSG ratios. Note that, even under fully reducing conditions (5 mM GSH), approximately 50% of αA-crystallin is oxidized, likely due to GSSG impurities. **e**) The same titration as in (**d**) using αA_{ox} at the reaction start. **f**) Relative intensities of αA_{red} and αA_{ox} monomer bands of gels as shown in (**d**) and (**e**) as a function of the $[GSH]^2$:[GSSG] ratio. Half-maximal oxidation (dashed line) at a redox potential of – 222 mV (black, K_{eq}: 257 mM) for αA_{red} and -224 mV (gray, K_{eq} 306 mM) for αA_{ox}. In (**a-f**), the shaded areas (green) indicate the lenticular $[GSH]^2$:[GSSG] redox potential range. In (**c**) and (**f**), values plotted are mean and s.d. of n=3 replicate determinations of one titration.

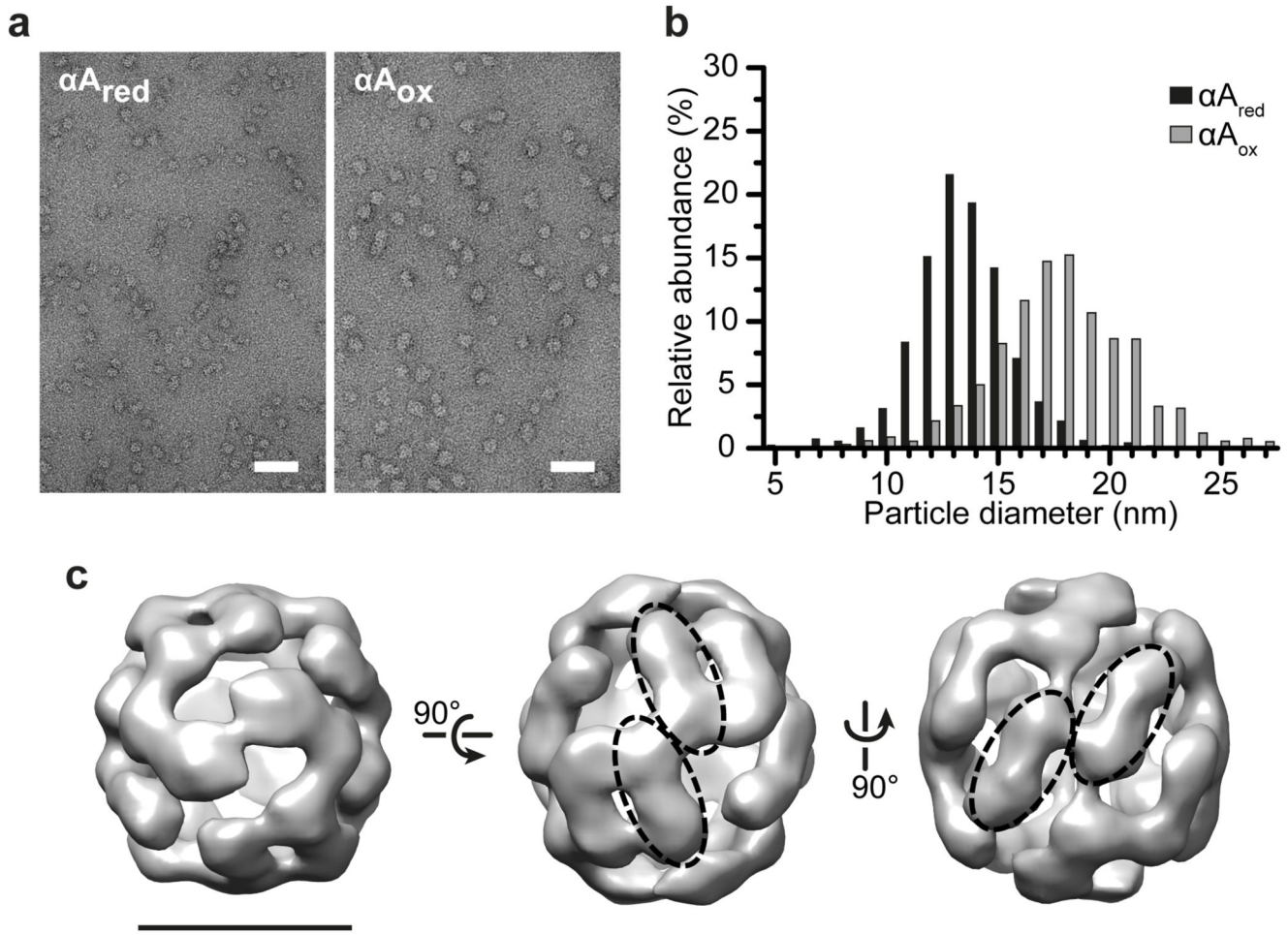

Figure 5. Oligomer architecture of oxidized human αA-crystallin.

a) Electron micrographs of αA_{red} (left) and αA_{ox} (right) oligomers negatively stained with 2% uranyl acetate. Scale bars: 50 nm. Note the increased oligomer size and polydispersity in αA_{ox}. **b**) Size distributions of the oligomers of αA_{red} (black bars) and αA_{ox} (gray bars). The average oligomer size is shifted from ~13.5 nm in αA_{red} to ~17.7 nm in αA_{ox}. **c**) Different views of the 3D-reconstruction of a 32-meric assembly of αA_{ox}. Scale bar: 10 nm. Dimeric building blocks are indicated by dashed ellipses.

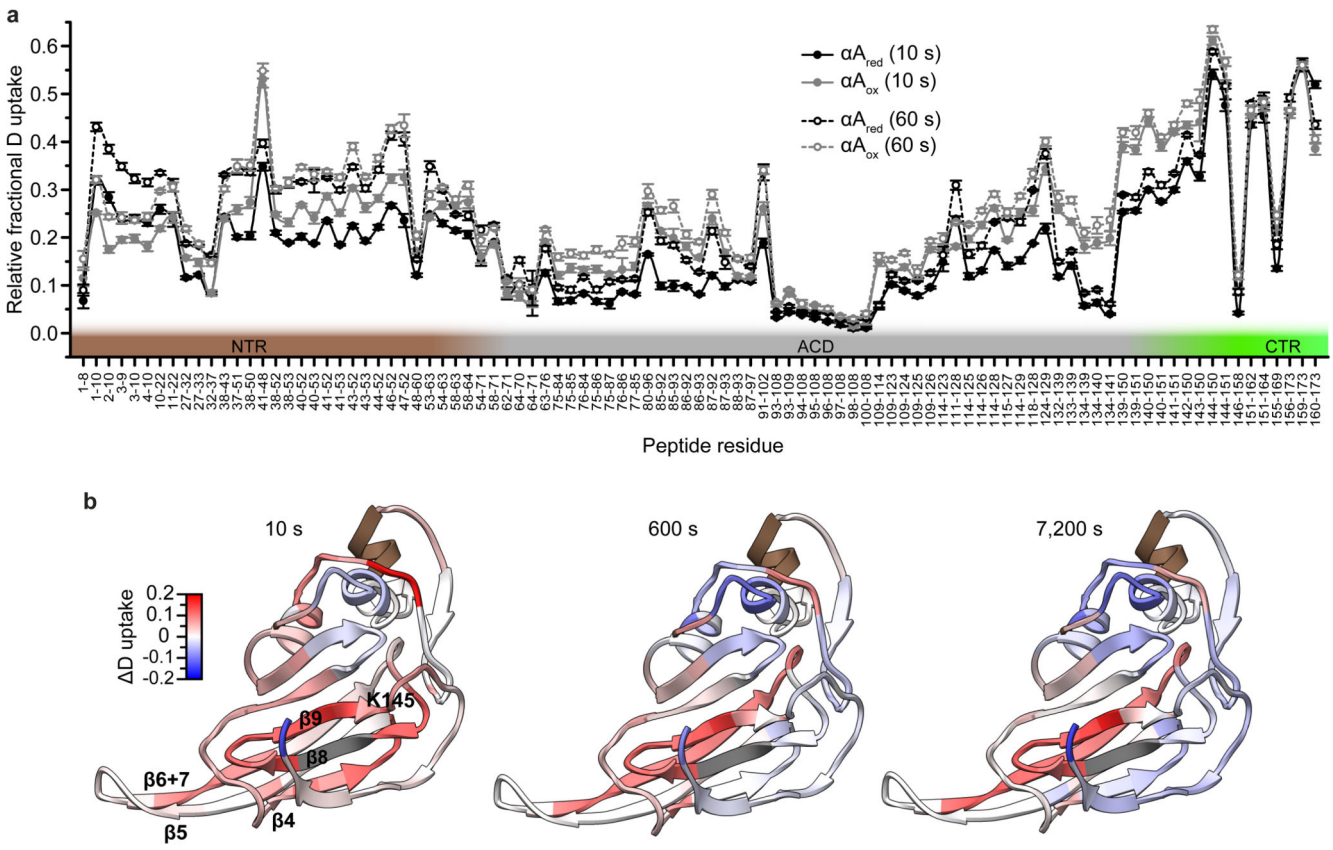

Figure 6. Dynamics of oxidized human αA-crystallin.

a) Relative fractional deuterium uptake of all peptides detected in H/DX-MS experiments. The deuteration behavior for early timepoints (10 s and 60 s) of the exchange reaction is shown. Peptides ordered by their midpoint; the peptide start and end amino acid positions are indicated at the abscissa. Note that the uptake pattern is overall well conserved among αA_{red} and αA_{ox}. Values plotted are means of n=3 technical replicates. The error bars reflect the corresponding s.d. **b**) Differences in amide hydrogen protection in αA_{red} and αA_{ox} mapped onto the model of a non-3D domain-swapped monomer of αA-crystallin. Differences in deuterium uptake were obtained by the difference in local relative deuterium uptake (ΔD uptake αA_{ox} - αA_{red}), averaged using the DynamX 3.0 (Waters). Regions in αA_{ox} with unchanged protection from deuteration are colored white, with decreased protection red, and with increased protection blue. Regions with insufficient coverage are colored according to the domain color code.

Europe PMC Funders Author Manuscripts

Europe PMC Funders Author Manuscripts

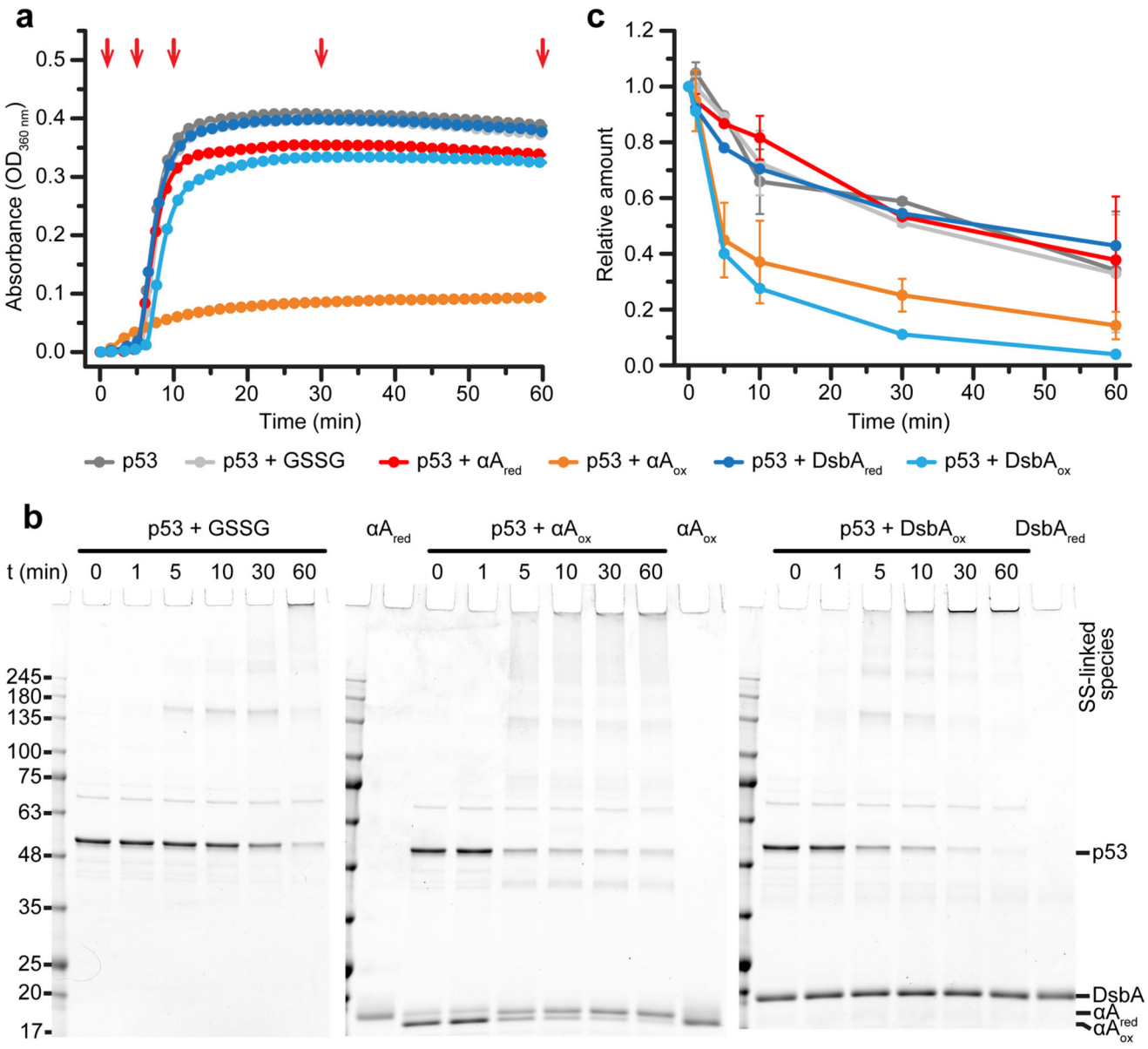

Figure 7. αA-crystallin is capable of transferring disulfide bonds to human p53.

a) Heat-induced aggregation of recombinant p53 (2 μM) in the presence of a twofold molar excess of GSSG, αA_{red}, αA_{ox}, reduced ($DsbA_{red}$) or oxidized ($DsbA_{ox}$) recombinant *E. coli* DsbA. Note that the aggregation of p53 is only suppressed in the presence of αA_{ox}. **b**) Non-reducing, denaturing PAGE of samples withdrawn at the indicated timepoints (red arrows) from the aggregation assays in the presence of GSSG, αA_{ox} or $DsbA_{ox}$ shown in (**a**). Note that disulfide-bridged species of p53 are formed both in the presence of αA_{ox} and $DsbA_{ox}$. Concomittantly, αA_{ox} loses its intramolecular disulfide bond. **c**) Relative intensity of the p53 monomer band as a fraction of the intensity (amount of monomer) at the beginning of each aggregation kinetics experiment (t = 0 min). Values are plotted as mean and s.d. of n=2 independent experiments.

Table 1

Cryo-EM data collection and validation statistics for αA-crystallin oligomer reconstructions.

	12-mer (D3) (EMD-4895)	16-mer (D4) (EMD-4894, PDB 6T1R)	20-mer (D5) (EMD-4896)
Data collection and processing			
Molecular mass (kDa)	238.9	318.5	398.2
Magnification	37,000	37,000	37,000
Voltage (kV)	300	300	300
Electron exposure (e^{-}/Å^2)	30	30	30
Defocus range (μm)	1.2-2.5	1.2-2.5	1.2-2.5
Pixel size (Å)	1.35	1.35	1.35
Symmetry imposed	D3	D4	D5
Initial particle images (no.)	74,068	74,068	74,068
Final particle images (no.)	26,596	19,783	14,336
Relative abundance (%)*	35.9	26.7	19.4
Map resolution (Å)	9.2	9.8	9.0
FSC threshold	0.143	0.143	0.143
Dimensions (width x height in Å)	10.8 x 13.6	10.9 x 13.8	12.0 x 13.7
Validation			
MolProbity score	-	2.23	-
Clashscore	-	17	-
Poor rotamers (%)	-	0	-
Ramachandran plot	-		-
Favored (%)	-	92	-
Allowed (%)	-	8	-
Disallowed (%)	-	1	-

*Relative abundance with respect to the total number of images in the initial cryo-EM dataset.